LUND UNIVERSITY

Numerical and experimental aspect of coherent lensless imaging

Malm, Erik

2021

Document Version:
Publisher's PDF, also known as Version of record

Link to publication

Citation for published version (APA):
Malm, E. (2021). *Numerical and experimental aspect of coherent lensless imaging*. Lund University.

Total number of authors:
1

LUND UNIVERSITY

PO Box 117
221 00 Lund
+46 46-222 00 00

Numerical and experimental aspects of coherent lensless imaging

ERIK MALM
DEPARTMENT OF PHYSICS | FACULTY OF SCIENCE | LUND UNIVERSITY

Numerical and experimental aspects of coherent lensless imaging

Numerical and experimental aspects of coherent lensless imaging

Erik Malm

DOCTORAL THESIS

To be presented, with the permission of the Faculty of Science of Lund University, for public criticism in Rydberg hall (Fysikum) at the Department of Physics on Wednesday, the 26th of May 2021 at 9:15.

Faculty opponent:
Dr. William Schlotter
Stanford University

Organization
LUND UNIVERSITY

Department of Physics
Division of Synchrotron Radiation Research
Box 118, S-221 00 Lund, Sweden

Document name
DOCTORAL DISSERTATION

Date of disputation
2021-5-26

Sponsoring organization

Author(s)
Erik Malm

Title and subtitle
Numerical and experimental aspects of coherent lensless imaging

Abstract

This thesis is devoted to the understanding, application, and extension of coherent lensless imaging methods for microscopy purposes. Particular attention is given to the Fourier transform holography and coherent diffractive imaging methods. These two methods share several properties such as the ability for singleshot imaging and their experimental geometries, but differ greatly in their reconstruction approach. Holographic approaches use reference waves to encode phase information into the measurements which means the reconstruction quality is controlled, to a large extent, by the characteristics of the reference wave. In contrast, coherent diffractive imaging utilizes prior knowledge to iteratively recover the phase information; this has the effect that the reconstruction quality is independent of any optics or references, but relies heavily on the performance of iterative numerical algorithms. The complex nature of the phase retrieval problem raises questions regarding the existence and uniqueness of a solution which makes understanding the numerical and mathematical aspects of the problem of central importance.

The main topics in this thesis include: the extension of coherent diffractive imaging to multi-wavelength diffraction data, effects related to optically thick references in Fourier transform holography and an alternative numerical approach to phase retrieval which is based on non-rigid image registration. Along the way, various topics are covered which form the foundations of these techniques, or could be useful to a practioner in the field.

Key words
Coherent diffractive imaging, holography, phase retrieval, diffraction, inverse scattering, XUV light, non-rigid image registration

Classification system and/or index terms (if any)

Supplementary bibliographical information

Language
English

ISSN and key title

ISBN
978-91-7895-873-3 (print)
978-91-7895-874-0 (pdf)

Recipient's notes

Number of pages
164

Price

Security classification

I, the undersigned, being the copyright owner of the abstract of the above-mentioned dissertation, hereby grant to all reference sources the permission to publish and disseminate the abstract of the above-mentioned dissertation.

Signature ______________________ Date 2021-4-20

Numerical and experimental aspects of coherent lensless imaging

Erik Malm

DOCTORAL THESIS

2021

Division of Synchrotron Radiation Research
Department of Physics
Lund University

Faculty of Science, Department of Physics

ISBN: 978-91-7895-873-3 (print)
ISBN: 978-91-7895-874-0 (pdf)

Printed in Sweden by Media-Tryck, Lund University, Lund 2021

Abstract

This thesis is devoted to the understanding, application, and extension of coherent lensless imaging methods for microscopy purposes. Particular attention is given to the Fourier transform holography and coherent diffractive imaging methods. These two methods share several properties such as the ability for singleshot imaging and their experimental geometries, but differ greatly in their reconstruction approach. Holographic approaches use reference waves to encode phase information into the measurements which means the reconstruction quality is controlled, to a large extent, by the characteristics of the reference wave. In contrast, coherent diffractive imaging utilizes prior knowledge to iteratively recover the phase information; this has the effect that the reconstruction quality is independent of any optics or references, but relies heavily on the performance of iterative numerical algorithms. The complex nature of the phase retrieval problem raises questions regarding the existence and uniqueness of a solution which makes understanding the numerical and mathematical aspects of the problem of central importance.

The main topics in this thesis include: the extension of coherent diffractive imaging to multi-wavelength diffraction data, effects related to optically thick references in Fourier transform holography and an alternative numerical approach to phase retrieval which is based on non-rigid image registration. Along the way, various topics are covered which form the foundations of these techniques, or could be useful to a practioner in the field.

Popular science summary

The resolution of an optical microscope is typically limited to a few hundred nanometers. The reason for this comes from the fact that the resolution is proportional to the wavelength of the light it uses. In principle, one way to improve the resolution is to use light with a smaller wavelength. Unfortunately, high-quality optics are difficult and expensive to fabricate especially for short-wavelength light such as extreme ultraviolet and X-rays. At these wavelengths, the optics can limit the resolution and may introduce image artifacts. Recently, however, a new set of techniques have emerged which removes the need for lenses. Coherent lensless imaging methods instead rely on coherent (laser) light and numerical algorithms.

The main difficulty associated with coherent lensless imaging stems from the way detectors measure light. From visible to X-ray regime, detectors can measure the wave's amplitude, but cannot directly measure its phase. This situation is analogous to being on the beach and having the ability to measure the height of the waves, but not when they arrive. This gives rise to the "phase problem". In general, there are a few ways to solve this problem.

Holographic methods introduce an additional reference wave which combines with the sample wave at the detector to produce interference fringes. These fringes are only visible because the incoming wave is coherent; otherwise, the fringes would become blurred and the corresponding information lost. This procedure converts phase information into amplitude variations which allows the detector to indirectly measure both quantities. Holographic methods are incredibly powerful, but now, the resolution and image quality is dictated by the characteristics of the reference wave. Studying the effects of the reference wave on the reconstruction is one of the topics covered in this thesis.

Another approach, coherent diffractive imaging, utilizes phase retrieval algorithms to recover the phase. These algorithms use knowledge about the sample (most commonly the shape and size) and the measured amplitude data to find a solution. Regarding the experimental setup, this approach provides the maximum amount of flexibility. Broadly speaking, coherent diffractive imaging removes experimental constraints by transferring them into numerical optimization problems.

Very often, a light source's spectrum will consist of several wavelengths. If the additional wavelengths are not removed, the interference pattern measured by the detector will become blurred. So, it is common to utilize optics to remove the unwanted spectrum leaving only a single wavelength. This procedure is necessary for most phase retrieval algorithms to work properly, but reduces the photon efficiency of the experiment. The development of new algorithms which can utilize multiple wavelengths is another aspect of this work. This could lead to higher efficiency experiments, but more importantly, may provide additional sample information and open up new experimental possibilities in the future.

List of papers

This thesis is based on the following papers which will be referred to by their Roman numerals.

I **Singleshot polychromatic coherent diffractive imaging with a high-order harmonic source**

E. Malm, H. Wikmark, B. Pfau, P. Villanueva-Perez, J. Peschel, S. Maclot, M. Schneider, S. Eisebitt, A. Mikkelsen, A. L'Huillier, P. Johnsson
Optics Express **28**(1), 394–404 (2020)

II **Multi-wavelength phase retrieval for coherent diffractive imaging**

E. Malm, E. Fohtung, A. Mikkelsen
Optics Letters **46**(1), 13–16 (2021)

III **Phase retrieval via non-rigid image registration**

E. Malm
In manuscript

IV **Reference shape effects on Fourier transform holography**

E. Malm, B. Pfau, M. Schneider, C. Günther, P. Hessing, F. Büttner, I. Lemesh, A. Mikkelsen, G. Beach, S. Eisebitt
In manuscript

V **2D and 3D nanoscale imaging using high repetition rate laboratory-based soft X-ray sources**

H. Stiel, A Blechshmidt, A Dehlinger, R. Jung, **E. Malm**, B. Pfau, C. Pratsch, C. Seim, J. Tümmler, M. Zürch
X-ray Lasers 2016, Proceedings of the 15th International Conference on X-Ray Lasers, 265-272 (2016)

All papers are reproduced with permission of their respective publishers.

Publications which I have contributed to, but are not included in this thesis:

Imaging Non-Local Magnetization Dynamics

C. von Korff Schmising, B. Pfau, M. Schneider, C. Günther, D. Weder, F. Willems, J. Geilhufe, **E. Malm**, L. Müller, B. Vodungbo, F. Capotondi, E. Pedersoli, M. Manfredda, J. Lüning, S. Eisebitt
Synchrotron Radiation News **29**, 26-31 (2016)

Single-shot extreme-ultraviolet wavefront measurements of high-order harmonics
H. Dacasa, H. Coudert-alteirac, C. Guo, E. Kueny, F. Campi, J. Lahl, J. Peschel, H. Wikmark, B. Major, **E. Malm**, D. Alj, K. Varjú, C. Arnold, G. Dovillaire, P. Johnsson, A. L'huiller, P. Rudawski, P. Zeitoun
Optics Express **27**, 2656-2670 (2019)

Abbreviations

The following abbreviations are used throughout this thesis.

2D, 3D	Two, three dimensional
CDI	Coherent diffractive imaging
ER	Error reduction algorithm
ESW	Exit surface wave
FTH	Fourier transform holography
HHG	High-order harmonic generation
HIO	Hybrid-input-output algorithm
SEM	Scanning electron microscope
SNR	Signal-to-noise ratio
XUV	Extreme ultraviolet

Notation

The following notation is used throughout this thesis.

x	Spatial coordinate in $\mathbb{R}^2$ or $\mathbb{R}^3$
$f \circ g$	Function composition
$\mathcal{F}$	Fourier transform operator
$f * g$	Convolution between functions
f^*	Complex conjugation
$v \cdot w \equiv v_i w^i$	Vector inner product
$f \times g$	Simple multiplication or vector cross product
$\mathbb{R}$	Real numbers
$\mathbb{R}_+ := \{x \in \mathbb{R} : x \geq 0\}$	Positive real numbers including zero
$\mathbb{S}^n := \{x \in \mathbb{R}^{n+1} : \|x\| = 1\}$	n-dimensional unit sphere
$\bar{\Omega}$	Closure of Ω
$\partial\Omega := \bar{\Omega}\backslash\Omega$	Boundary of Ω
$\|f\|_{L^p(\Omega)}$	L^p-norm of f on the domain Ω

Colormaps

The following colormaps are used throughout the thesis.

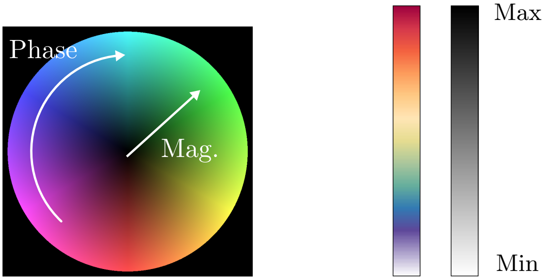

Figure 1: (Left) Colormap used to visualize complex-valued images where the magnitude and phase are mapped to intensity and hue within the image.

Contents

1 Introduction 1

2 Classical electrodynamics and diffraction theory 5
2.1 Electrodynamics . . . 5
2.2 Scalar diffraction . . . 7
  2.2.1 Projection approximation . . . 9
  2.2.2 Born approximation . . . 10
  2.2.3 Diffraction from a thin screen . . . 11
2.3 Charge and magnetic scattering . . . 13
2.4 Multislice propagation method . . . 15

3 Short-wavelength light sources 17
3.1 High-harmonic generation . . . 17
3.2 Lasers . . . 18
3.3 Synchrotron radiation . . . 19

4 Coherent lensless imaging 21
4.1 Fourier transform holography . . . 22
  4.1.1 Missing beamstop data . . . 24
4.2 Coherent diffractive imaging . . . 25
  4.2.1 Uniqueness . . . 28
  4.2.2 Dynamic support and solution selection . . . 30
4.3 Thick samples and references . . . 32

5 Multi-wavelength coherent diffractive imaging 37
5.1 Partial coherence . . . 38
5.2 Multi-wavelength phase retrieval . . . 41
5.3 Vector CDI for magnetic samples . . . 46

6 Image registration for phase retrieval 49
6.1 Registration Theory . . . 50
6.2 Numerical performance . . . 52
6.3 Extensions . . . 53

7 Summary and outlook 57
7.1 Phase retrieval on arbitrary closed surfaces . . . 58

A Differential forms 61

Bibliography 63

Summary of Papers 79

1

Introduction

Coherent lensless imaging is a collection of microscopy techniques which replace the image-forming optics found within conventional microscopes with numerical algorithms. A major motivation for this shift stems from the difficulty associated with fabricating high-quality optics for short-wavelength[1] light. Low-quality optics limit a microscope's resolution and can introduce image artifacts. In addition, the image contrast is typically sensitive to the sample's absorption requiring additional techniques for obtaining phase contrast. In contrast, coherent lensless imaging techniques recover the entirety of the wavefield making them sensitive to both phase and absorption. And, due to the lack of optics, the spatial resolution is no longer limited by the numerical aperture of the optics but by the wavelength and maximum scattering angle of the measurements.

The primary difficulty associated with a coherent lensless imaging experiment is the so-called "phase problem" which results from the fact that detectors can only measure a wavefield's amplitude. Once the phase has been recovered, the wave can be numerically back-propagated from the detector to the sample plane. The wave immediately following the sample, or exit surface wave (ESW), can be related to specific sample properties such as: material thickness, electron or spin density or strain.

There are two general schemes used to recover the phase; holographic methods utilize a known reference wave to encode phase information into the intensity measurements while other methods rely more heavily on numerical algorithms. In holography a known reference wave interferes with the sample wave to produce a modulated intensity pattern. The reconstruction procedure is deterministic and fast to com-

---

[1] Herein "short-wavelength" refers to the extreme ultraviolet (5 nm–50 nm) and soft X-ray (0.5 nm–5 nm) wavelengths.

pute, but the signal-to-noise ratio (SNR) and resolution are limited by the reference wave. In the short-wavelength regimes, in-line holography [1] and Fourier transform holography (FTH) are most commonly used.

An alternative approach is to use iterative algorithms to perform phase retrieval which use measurements of the sample's diffraction pattern and additional information to recover the phase. Iterative phase retrieval algorithms tend to be computationally and theoretically more complicated than holographic methods, but allow for simpler experimental setups and potentially higher spatial-resolution. On the other hand, the complicated theoretical aspects means that the existence or uniqueness of a solution is not guaranteed. These issues become more pronounced when the measurements contain noise or missing data. Experiments which acquire diffraction measurements and utilize iterative phase retrieval methods will be referred to as coherent diffractive imaging (CDI). CDI is actually comprised of several approaches or geometries such as: plane-wave CDI [2, 3, 4], Fresnel CDI [5], Bragg CDI [6, 7, 8, 9, 10] or ptychography [11, 12]. This thesis is concerned primarily with the plane-wave CDI[2] and FTH methods.

Short-wavelength coherent lensless imaging is a relatively new field, in part, due to the recent increased availability of bright coherent sources and computational resources. In 1972, Gerchberg and Saxton proposed a phase retrieval algorithm which utilized image amplitude information from both the sample and detector planes [13]. This was followed by Fienup who demonstrated phase retrieval numerically using the support[3] of the function and its amplitude in Fourier space [14]. These algorithms laid the foundation for the majority of iterative phase retrieval algorithms which are used today. In 1999, Miao et al. demonstrated CDI experimentally for the first time [2]. Around the same time, X-ray FTH was being developed as a high-resolution imaging method [15] and in 1992, McNulty et al. [16] demonstrated X-ray FTH using the first-order focus from a Fresnel zone plate as the reference wave. This was followed by Eisebitt *et al.* in 2004 [17] which used a small pinhole, fabricated within the sample mask, to create the reference wave; this has the added benefit that the sample and reference are mechanically coupled which results in additional stability. Since then, a number of experiments have utilized FTH and CDI for imaging samples on the nanoscale. Nowadays, CDI and FTH are used to study a variety of different samples ranging from biological [18, 19, 20, 21, 22] to magnetic thin films [17, 23, 24, 4].Quality reviews of these topics can be found in [25, 26, 9, 27, 28, 29, 30, 31, 32, 33].

This thesis is composed of two parts, the first half introduces the underlying theory and presents a summary of the papers. This is followed by the papers themselves in the second half. Starting from Maxwell's equations, Chapter 2 introduces the relevant concepts of scalar diffraction theory. These concepts provide the tools necessary to understand wave propagation and the inversion methods used throughout the rest of the thesis. This is followed by an introduction to different types of short-wavelength light sources in Chapter 3. The first two sections of Chapter 4

---

[2] Throughout the thesis "plane-wave CDI" and "CDI" will be used interchangeably.

[3] The region where the function is non-zero.

describe the basic 2D theory behind the FTH and CDI methods and some common complications which may arise in an experiment. At the end of the chapter, an overview of Paper IV is provided which studies the effects of using optically thick reference apertures on the FTH reconstruction. Chapter 5 gives an overview of the work presented in Papers I and II which are concerned with extending CDI to include multi-wavelength sources. In Chapter 6 and Appendix A, the underlying concepts related to Paper III are introduced. Here, non-rigid image registration is developed as a method for phase retrieval. The method starts with an initial guess and then looks for a transformation that warps this guess until its diffraction pattern matches the data. Lastly, in Chapter 7, concluding remarks and discussion on potential future directions are provided. The discussion is facilitated by an example which considers the extension of phase retrieval to 3D surfaces.

2

Classical electrodynamics and diffraction theory

Methods for solving inverse problems rely on a clear understanding of the forward problem. Here, the forward problem is: given a known incident field and sample, find the resulting diffracted (scattered) field. The inverse problem consists of using the diffraction measurements to recover certain properties about the sample. In this thesis, "diffraction" is used in a broad sense to mean any deviation from geometrical optics provided the sample dimensions are large compared to the wavelength. This chapter is devoted to the development of scalar diffraction theory starting from Maxwell's equations. The concepts developed in this chapter are based primarily on the treatments in [34, 35, 36, 37].

2.1 Electrodynamics

Our starting point[1] will be the set of Maxwell's equations which govern classical electromagnetism[2] and provide local relationships between the electric, E, and magnetic, H, fields to the charge, ρ, and current, J, densities throughout space and

---

[1] We could start with the more general relativistic equations involving the electromagnetic field tensor, f, given by $df = 0$ and $\delta f = j$ (in Gaussian units with metric signature: $(- + ++)$) or a Lagrangian formulation, but little would be gained in our context.

[2] Together with the Lorentz force equation: $F = q(E + v \times B)$.

time. Maxwell's equations are given by

$$\nabla \cdot D = \rho \tag{2.1}$$

$$\nabla \cdot B = 0 \tag{2.2}$$

$$\nabla \times H - \partial_t D = J \tag{2.3}$$

$$\nabla \times E + \partial_t B = 0\,, \tag{2.4}$$

where the dependence on the time, $t \in \mathbb{R}$, and spatial, $x \in \mathbb{R}^3$, coordinates are implicit. The electric displacement, D, is related to the electric field and the polarization of the material, P, through the equation $D = \epsilon_0 E + P$. Similarly, the relationship between the magnetic field, H, magnetic induction, B and the magnetization, M, is given by $H = \frac{1}{\mu_0}B - M$. We can transform the set of coupled first order differential equations involving vector fields[3] into decoupled equations for scalar fields (scalar Helmholtz equation) by making a few simplifications.

We will consider a source-free region of space with materials that are non-magnetic, linear and isotropic such that the following simplifications can be made:

$$\rho,\, J \to 0 \tag{2.5}$$

$$\bar{\bar{\mu}}\,(x) \to \mu_0 \tag{2.6}$$

$$\bar{\bar{\epsilon}}\,(x) \to \epsilon\,(x) \tag{2.7}$$

$$D(x,t) \to \epsilon(x)\,E(x,t) \tag{2.8}$$

$$B(x,t) \to \mu_0 H(x,t)\,. \tag{2.9}$$

Above, μ_0 is the vacuum permeability and ϵ is the, now scalar, material permittivity. Already, these simplifications have excluded phenomena related to magnetism and nonlinear optics. In fact, high-order harmonic generation (HHG) sources described in Chapter 3 rely on the nonlinear dependence of the polarization on the electric field: $P_i = \epsilon_0(\chi^{(1)}_{ij}E^j + \chi^{(2)}_{ijk}E^jE^k + \dots)$[4]. The relevant theory related to these areas will be reinserted in an ad hoc fashion as they are needed in later sections.

The time dependence can be removed from Maxwell's equations by replacing the time-dependent fields with their Fourier representations in the frequency domain, ω, through[5]

$$E(x,t) = \frac{1}{2\pi}\int_{\mathbb{R}} E(x,\omega)e^{-i\omega t}d\omega\,. \tag{2.10}$$

Likewise, the same Fourier representation can be made for $H(x,t)$. Substitution of the Fourier representations of E and H into Maxwell's equations and treating each

---

[3] Note that we do not use bold letters or any other notation to differentiate vector fields from scalar fields, instead we rely on the context and try to remember that E, D, H, B, J are vector fields, or equivalently: $E, D, H, B, J:\ \mathbb{R}^3 \times \mathbb{R} \to \mathbb{R}^3$.

[4] The Einstein summation convention is used throughout the thesis for repeated indices such that $v^i w_i \equiv \sum_i v^i w_i$.

[5] The form of (2.10) means we need to remember to include the negative frequencies to ensure that $E(x,t)$ is real $(\delta\,(\omega) \to \delta\,(-\omega) + \delta\,(\omega))$.

Fourier component separately[6] we arrive at a set of simplified equations

$$\nabla \cdot (\epsilon E) = 0 \tag{2.11}$$

$$\nabla \cdot B = 0 \tag{2.12}$$

$$\nabla \times H + i\omega\epsilon E = 0 \tag{2.13}$$

$$\nabla \times E - i\omega B = 0\,, \tag{2.14}$$

where the quantities have become complex valued. When $\epsilon(x)$ is a slowly varying function in space, the first equation can be approximated using

$$\nabla \cdot (\epsilon E) = E \cdot \nabla\epsilon + \epsilon\nabla \cdot E \sim \epsilon\nabla \cdot E\,. \tag{2.15}$$

Taking the curl of (2.14) and using the identity $\nabla \times \nabla \times E = \nabla(\nabla \cdot E) - \nabla^2 E$, we obtain the Helmholtz equation for the electric field. Then, by selecting a single component we arrive at the familiar scalar Helmholtz equation

$$\Delta u + k^2 u = 0\,, \tag{2.16}$$

where $u = E^i$ and $\Delta = \nabla^2 \equiv \nabla \cdot \nabla$ is the Laplacian operator. The wavenumber, $k = \sqrt{\mu\epsilon}\,\omega$, is related to the index of refraction, n, and the vacuum wavenumber, k_0, through $k = nk_0$. The index of refraction in terms of ϵ and μ is given by

$$n = \sqrt{\frac{\mu\epsilon}{\mu_0\epsilon_0}}\,. \tag{2.17}$$

In the X-ray regime, the index of refraction is often written as $n = 1 - \delta + i\beta$, where δ and β are dependent on ω. For X-rays, n often deviates only slightly from 1 allowing for the following approximation

$$1 - n^2 \sim 2\left(\delta - i\beta\right)\,. \tag{2.18}$$

to be made. The effect which δ and β have on an incident wave is described in Section 2.2.1.

2.2 Scalar diffraction

The aim of this section is to develop integral expressions for u when an incident field scatters off an obstacle and is observed at a point x. The solution to the interior problem will be calculated and used to find the solution to the exterior problem as this geometry is more relevant to our experiments. The geometries associated with the two problems are shown in Fig. 2.1. Smoothness requirements for the functions and domains are neglected here, but can be found in the more complete and careful treatments of the subject in [37, 38]. Starting from Green's second theorem, we find that

$$\int_\Omega \left(u\Delta v - v\Delta u\right) dx' = \int_{\partial\Omega} \left(u\frac{\partial v}{\partial n(x')} - v\frac{\partial u}{\partial n(x')}\right) dx'\,, \tag{2.19}$$

---

[6] The, now linear, material parameters allow us to treat each Fourier component separately.

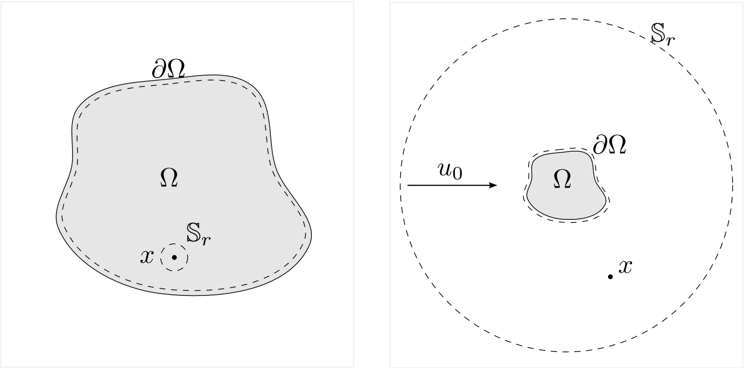

Figure 2.1: (Left) Interior problem where $x \in \Omega$ and (right) the exterior problem where $x \in \mathbb{R}^3\backslash\bar{\Omega}$.

where Ω and $\partial\Omega$ denote a bounded domain and its boundary in $\mathbb{R}^3$, we find the interior solution ($x \in \Omega$) by substituting the fundamental solution[7]

$$\Phi_k(x,x') = \frac{e^{ik|x-x'|}}{4\pi|x-x'|} \qquad x \neq x' \tag{2.20}$$

in for v. The singularity of $\Phi_k(x,x')$ at $x = x'$ is avoided by excluding a small spherical volume with radius r around the point x and taking the limit as the radius goes to zero. Both u and Φ_k satisfy the Helmholtz equation for free space making the left hand side in (2.19) vanish. We obtain an additional spherical boundary, $\mathbb{S}_r$, such that $\partial\Omega \to \partial\Omega \cup \mathbb{S}_r$. Taking $\lim r \to 0$ we find

$$u(x) = \int_{\partial\Omega} \left(\Phi_k(x,x')\,\frac{\partial u(x')}{\partial n(x')} - u(x')\,\frac{\partial \Phi_k(x,x')}{\partial n(x')} \right) dx' \tag{2.21}$$

for $x \in \mathbb{R}^3\backslash\partial\Omega$. Making use of the single, $\mathcal{S}_k$, and double, $\mathcal{D}_k$, layer potentials defined by

$$\mathcal{S}_k\varphi\,(x) := \int_{\partial\Omega} \Phi_k(x,x')\,\varphi(x')\,dx' \qquad x \in \mathbb{R}^3\backslash\partial\Omega \tag{2.22}$$

$$\mathcal{D}_k\varphi\,(x) := \int_{\partial\Omega} \frac{\partial \Phi_k(x,x')}{\partial n(x')}\,\varphi(x')\,dx' \qquad x \in \mathbb{R}^3\backslash\partial\Omega, \tag{2.23}$$

the interior solution can be rewritten in the compact form

$$u(x) = \mathcal{S}_k \partial_n^- u - \mathcal{D}_k \gamma^- u \qquad x \in \Omega\,, \tag{2.24}$$

where γ^-, ∂_n^- are the (interior) Dirichlet and Neumann traces respectively[8].

---

[7] Where the fundamental solution (Green's function) is the solution to $\left(\Delta + k^2\right)\Phi_k\left(x,x'\right) = -\delta\left(x - x'\right)$.

[8] The Dirichlet trace is defined as $\gamma^\pm u(x) := \lim\limits_{y\to x,\, y\in\Theta^\pm(x)} u(y)$ where $\Theta^\pm(x)$ is a non-tangential path to x from the exterior (+) or interior (−). Similarly for the Neumann trace $\partial_n^\pm u(x) := \lim\limits_{y\to x,\, y\in\Theta^\pm(x)} n(x)\cdot\nabla u(y)$

The solution to the exterior problem can be obtained from (2.24) by viewing it as an interior problem with outer boundary, $\mathbb{S}_r$, located at infinity (Fig. 2.1) such that the radius, $r = |x| \to \infty$, and by considering only fields that satisfy the Sommerfeld radiation condition

$$\lim_{r\to\infty} r\left(\frac{\partial u}{\partial r} - iku\right) = 0\,. \tag{2.25}$$

This requirement ensures that the fields are outgoing waves at infinity. The contribution from $\mathbb{S}_r$ vanishes[9] and we find the solution to the exterior problem is given by[10]

$$u(x) = -\mathcal{S}_k\partial_n^+ u + \mathcal{D}_k\gamma^+ u \qquad x \in \mathbb{R}^3\backslash\bar{\Omega}\,. \tag{2.26}$$

This equation provides a relationship between the field in the exterior of the sample to itself and its normal derivative evaluated on the boundary of the obstacle (the Cauchy data, $c_+u = (\gamma^+ u, \partial_n^+ u)^T$). A detailed derivation can be found in [37]. Finding the solution of the boundary integral equation in (2.26) is quite involved and can be computationally expensive especially for high frequencies. We would like to make further simplifications to (2.26) so we can calculate reasonable approximate solutions with modest effort. The iterative algorithms described in later chapters rely on solving for u hundreds to thousands of times which makes it well worth our time to find simplified expressions.

2.2.1 Projection approximation

The most common way to describe the sample's effect on the incident field is through the projection approximation. This approximation neglects diffraction and multiple scattering effects resulting in a simple expression for the transmitted field. In effect, the 3D sample is projected along the incident field direction allowing it to be treated as a 2D transmission function. This approximation is the key relation used by reconstruction algorithms (e.g. back-projection or algebraic reconstruction techniques) for X-ray tomography [39]. The projection approximation can be derived from (2.16) by decomposing the field into an envelope function, v, and a z-directed plane wave which takes the form

$$u(x, z) = v(x, z)e^{ikz}\,, \tag{2.27}$$

where x is a coordinate in the two-dimensional plane orthogonal to the z-axis. Neglecting second order derivatives on v (2.16) becomes

$$\partial_z v(x, z) \sim \frac{-ik_0}{2}\left(1 - n^2(x, z)\right) v(x, z)\,. \tag{2.28}$$

---

[9] It is important to note that the field itself does not vanish on this surface; otherwise, the field would vanish everywhere.

[10] The flipping of the normal vector $n \to -n$ is responsible for the change in sign between (2.24) and (2.26).

Then, solving for v yields a solution for u in terms of the incident field, u_0, given by

$$u(x, z = \Delta) = t_z(x)\, u_0(x)\,, \tag{2.29}$$

where the sample transmission function is specified by

$$t_z(x) = \exp\{\frac{-ik_0}{2} \int_0^\Delta \left[1 - n^2(x,z)\right] dz\} \tag{2.30}$$

$$\sim \exp\{k_0 \int_0^\Delta \left[-i\delta(x,z) - \beta(x,z)\right] dz\}\,. \tag{2.31}$$

The subscript in t_z indicates the direction of the incident field (projection direction). From (2.31) we can see that δ influences the phase while β is related to the sample's absorption.

2.2.2 Born approximation

A useful approximation can be made when the incident wave weakly interacts with the sample. This happens when $n \sim 1$ such that the electric field deviates only slightly from the incident field, $u \sim u_0$. In this situation, it is helpful to rewrite the Helmholtz equation (2.16) in the form

$$\left(\Delta + k_0^2\right) u = k_0^2 \left(1 - n^2\right) u\,, \tag{2.32}$$

where the right hand side is viewed as a small perturbation source term. Substituting u_0 for u on the right hand side we obtain the first-order Born approximation

$$u_1(x) = k_0^2 \int_\Omega \Phi_{k_0}(x, x') m(x') u_0(x') dx' \tag{2.33}$$

where $m := n^2 - 1$. Higher order approximations can be obtained in a recursive manner resulting in the Born series approximation

$$u = u_0 + u_1 + u_2 + \dots\,. \tag{2.34}$$

It is common to refer to the terms up to first order simply as the Born approximation.

For observation points which are far from the sample ($|x| \gg |x'|$) the fundamental solution can be approximated by

$$\Phi_k\left(x, x'\right) \sim \frac{e^{ik|x|}}{4\pi|x|} e^{-ik\hat{x}\cdot x'}\,. \tag{2.35}$$

Furthermore, let the incident field be a plane wave $u_0 = e^{ik_0 d\cdot x}$ traveling along the incident direction, $d \in \mathbb{S}^2$. Then, we can write the far-field first-order Born approximation as

$$u_\infty(\hat{x}) = k_0^2 \int_{\mathbb{R}^3} m(x')\, e^{-ik_0(\hat{x}-d)\cdot x'} dx'\,, \tag{2.36}$$

where $u_1 = \frac{e^{ik|x|}}{4\pi|x|}u_\infty$. Equation (2.36) can be viewed as a 3D Fourier transform of the sample evaluated at points that lie on the Ewald sphere given by $k = k_0(\hat{x}-d)$[11]. With $\hat{x}, d \in \mathbb{S}^2$ we can see that k_0 is the radius of the Ewald sphere. In experiment, data is collected in the forward direction using a finite-size detector which results in data that lie on a subset of the Ewald sphere. Separating the integration into components that are parallel and orthogonal to d we find

$$u_\infty(\hat{x}) = k_0^2 \int_{\mathbb{R}^2} \{ \int_{\mathbb{R}} m(x') e^{-ix'_d k_0 (\hat{x}-d)\cdot d} \, dx'_d \} \, e^{-ik_0(\hat{x}-d)_\perp \cdot x'_\perp} \, dx'_\perp \,, \tag{2.37}$$

where $x'_d = x' \cdot d$. When the sample is sufficiently thin and for small observation angles, the far field becomes

$$u_\infty(\hat{x}) = k_0^2 \int_{\mathbb{R}^2} m_d(x'_\perp) \, e^{-ik_0(\hat{x}-d)_\perp \cdot x'_\perp} dx'_\perp \,, \tag{2.38}$$

where $x_\perp$ indicates the components of x orthogonal to d. In this case, the far-field is proportional to the Fourier transform of the sample projected along the incident field direction. In terms of the Fourier transform operator, we find that

$$u_\infty \propto \mathcal{F}\{m_d\} \,, \tag{2.39}$$

where m_d is the projection of $n^2 - 1$ along the d-direction. This suggests that in order to recover the sample's index of refraction in 3D, a series of images need to be collected with varying incident angles as is done in tomography. In the context of 3D imaging with CDI, a discussion provided by Pierre Thibault [40] in response to an article [41] provides important insights into the phase retrieval method. In summary, one cannot invert the sample in three-dimensions from data lying only on the Ewald sphere unless significant amount of knowledge about the sample is known beforehand. In order to obtain more information, multiple wavelengths or projections must be used; this, however, does not necessarily exclude the possibility of singleshot 3D imaging [42, 43]. Alternatively, if the incident wave interacts strongly with the sample than additional information is available due to multiple scattering events. In this case, a full inversion of the data would need to be performed.

2.2.3 Diffraction from a thin screen

Additional simplifications can be made for thin samples which are located within openings of an opaque screen. Following the reasoning developed in [44], we will consider a sample to be optically thin when its thickness, Δ, satisfies the constraint:

$$\Delta < \frac{\lambda}{2\mathrm{NA}^2} \,, \tag{2.40}$$

where NA denotes the numerical aperture. This relationship can be determined by comparing the departure of the Ewald sphere from a flat plane with the speckle size in the incident direction.

---

[11] Here, k, is used to denote both the wavenumber and wavevector; the distinction should be clear from the context.

The geometry associated with a thin screen diffraction experiment is depicted in Fig. 2.2. The boundary is composed of two parts: the boundary located "at infinity", Γ_∞, and Γ located at the exit surface of the screen. The contribution from Γ_∞ vanishes leaving only the contribution from the apertures within the screen. The single layer potential in (2.26) and (2.19) can be removed by modifying Φ_k such that it vanishes on the screen ($z = 0$). This is accomplished through the method of images by using $\Phi_k^{Dir} = \Phi_k(x, x') - \Phi_k(x, x'')$ where the point x'' is the mirror image of x' about $z = 0$ such that $x'' = x'(z \to -z)$. Equation (2.19) becomes[12]

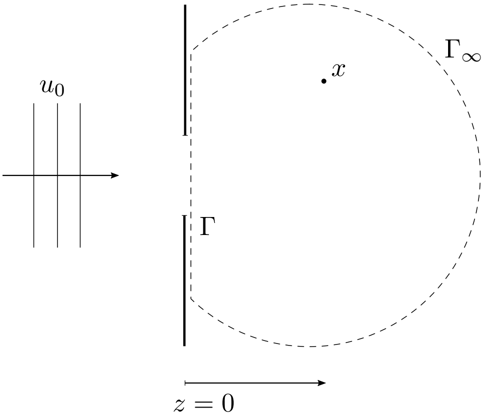

Figure 2.2: Geometry associated with diffraction from a thin screen.

$$u(x) = -2ik \int_\Gamma \Phi_k(x, x') \left(1 + \frac{i}{k|x - x'|}\right) \cos\theta\, u(x')\, dx' \tag{2.41}$$

where θ is the angle between n (z-axis typically) and the vector $x - x'$.

It is convenient to adopt a new set of coordinates to accommodate our simplified geometry. In the remaining part of this section, x and x' are used as two-dimensional coordinates which lie in the plane orthogonal to the z-axis such that $x \to (x, z)$.

For measurements collected far from the sample, (2.41) can be simplified using the paraxial approximation $|x - x'| \ll z$. With this simplification in hand, we can approximate $|x - x'|$ in (2.41)[13] using the Taylor expansion $\sqrt{(x - x')^2 + z^2} \sim z + \frac{1}{2z}(x - x')^2$. Then, Φ_k from (2.20) becomes

$$\Phi_k(x, x') \sim \frac{e^{ikz}}{4\pi z} \times e^{\frac{ik}{2z}(x - x')^2}. \tag{2.42}$$

We can simplify the expression in (2.41) further for small observation angles, $\cos\theta \sim 1$. If the observation distance, $|x|$, is large compared to λ then $|\frac{i}{k|x-x'|}| \ll 1$

---

[12] Using the relation: $\nabla_{x'}|x - x'| = -\frac{x - x'}{|x - x'|}$.

[13] Where x and x' still represent points in $\mathbb{R}^3$.

and the second term in (2.41) can also be neglected. Rewriting (2.41) using these simplifications results in the Fresnel equation

$$u(x) = \frac{e^{ikz}}{i\lambda z}\Psi(x)\int_\Gamma u\left(x'\right)\Psi(x')e^{\frac{-ik}{z}x\cdot x'}dx' \,, \tag{2.43}$$

where Ψ is a quadratic phase defined by $\Psi(x) = e^{\frac{ikx^2}{2z}}$. Further simplifications can be made when the observation points are located far from the sample or equivalently when $\frac{\pi}{\lambda}D^2 \ll z$, where D is the characteristic size of the sample. After making this approximation we arrive at the Fraunhofer or far-field equation

$$u(x) = \frac{e^{ikz}}{i\lambda z}\Psi(x)\int_\Gamma u(x')e^{\frac{-ik}{z}x\cdot x'}dx' \,. \tag{2.44}$$

Making the identification $q = \frac{x}{\lambda z}$, we can see that equations (2.43) and (2.44) involve a 2D Fourier transformation defined as

$$\tilde{u}(q) = \int_{\mathbb{R}^2} u(x')e^{-i2\pi q\cdot x'}dx' \,, \tag{2.45}$$

where $q \in \mathbb{R}^2$ are the spatial frequencies. Numerically, the Fourier transform operator, $\mathcal{F}$, is implemented using a 2D discrete Fourier transform of the form

$$\tilde{u}_{kl} = \sum_{m=0}^{M-1}\sum_{n=0}^{N-1} u_{mn}\, \exp\{-2\pi i\left(\frac{mk}{M}+\frac{nl}{N}\right)\} \,. \tag{2.46}$$

Rearranging the pixels, u_{mn} can be treated as a the complex-valued vector. Then, the discrete Fourier transform becomes a matrix operator $\mathcal{F} : \mathbb{C}^{M\cdot N} \to \mathbb{C}^{M\cdot N}$.

Using the Fourier transform operator, the far field[14] can be rewritten in terms of $\tilde{u}$ as

$$\hat{u}(y) = \frac{1}{\lambda z}\,\tilde{u}\circ\varphi^{-1}(y) \,, \tag{2.47}$$

where $\varphi^{-1}(y) = \frac{y}{\lambda z}$. Numerically, the distinction between $\hat{u}$ and $\tilde{u}$ is often unnecessary for monochromatic sources, but it becomes critical for understanding multi-wavelength coherent imaging (Chapter 5). Now, we have a simple and fast numerical method, involving the 2D discrete Fourier transform, for calculating the far field.

2.3 Charge and magnetic scattering

Next, we investigate the scattering of a transverse wave from a source that is small compared to λ. The largest contributions arise from the electric and magnetic dipole moments and the electric quadrupole moment. For a linearly polarized incident

---

[14] Neglecting phase factors.

wave, the scattered wave from the electric and magnetic dipoles obtain orthogonal polarizations which prevents them from interfering. For circularly polarized light however, the polarization is preserved which allows for interference to occur. This idea is the basic principle which used by current modern techniques to image magnetic samples [45, 17]. The derivations in this section follow the semi-classical treatments in [34, 46].

The retarded solution for the vector potential[15], A, in the Lorenz gauge for a given current density is given by

$$A(x) = \mu_0 \int_{\mathbb{R}^3} \Phi_k(x, x') J(x') dx' \,. \tag{2.48}$$

Expanding Φ_k using the approximation from (2.42) and expanding in powers of k we find

$$A(x) = \frac{\mu_0}{4\pi} \frac{e^{ik|x|}}{|x|} \sum_{n=0} \frac{(-ik)^n}{n!} \int_{\mathbb{R}^3} J(x')(\hat{x} \cdot x')^n dx' \,. \tag{2.49}$$

Considering the first term and making use of integration by parts, the continuity equation and the definition of the electric dipole moment, p, we find

$$\int_{\mathbb{R}^3} J(x') dx' = -\int_{\mathbb{R}^3} x' \cdot (\nabla_{x'} \cdot J(x')) dx' = -i\omega\, p \,. \tag{2.50}$$

We can see that the lowest order term for the vector potential is proportional to the electric dipole moment

$$A(x) = \frac{-i\omega\mu_0}{4\pi} \frac{e^{ik|x|}}{|x|}\, p \,. \tag{2.51}$$

The next order term ($n = 1$) results in a J which can be decomposed into symmetric and anti-symmetric terms resulting in electric quadrupole and magnetic dipole terms with the magnetic dipole term given by

$$A(x) = \frac{ik\mu_0}{4\pi} \frac{e^{ik|x|}}{|x|} (\hat{x} \times m) \,. \tag{2.52}$$

The quadrupole and higher order terms will be neglected and instead we will focus on only the dipole terms. For a transverse incident wave propagating along the $\hat{x}$-direction we find that $B = ik\; \hat{x} \times A$ and $E = -\frac{1}{\sqrt{\mu\epsilon}}\, \hat{x} \times B$. Then, the scattered electric fields from electric and magnetic dipole moments become

$$E_p = ck^2 \frac{Z_0}{4\pi} \frac{e^{ik|x|}}{|x|} (\hat{x} \times p) \times \hat{x} \tag{2.53}$$

$$E_m = -k^2 \frac{Z_0}{4\pi} \frac{e^{ik|x|}}{|x|} (\hat{x} \times m) \,, \tag{2.54}$$

---

[15] The vector potential being related to the magnetic flux density through: $B = \nabla \times A$.

where $Z_0 = \sqrt{\mu_0/\epsilon_0}$. For induced electric and magnetic dipole moments described by $p = -\frac{e^2}{m_e\omega^2}E$ and $m = i\frac{e^2\hbar\mu_0}{\omega m_e^2}(s \times B)$ [46], where e, m_e and s are the electron's charge, mass and spin respectively, we find the scattered fields become

$$E_p = -\alpha\,(\hat{x} \times E) \times \hat{x} \tag{2.55}$$

$$E_m = i\alpha\beta\,[s \times (d \times E)] \times \hat{x}\,. \tag{2.56}$$

In these expressions, the incident field direction is denoted by d, with $\hat{x}$ the observation direction, $\alpha := \frac{1}{4\pi\epsilon_0}\frac{e^2}{m_e c^2}\frac{e^{ik|x|}}{|x|}$ and $\beta := \frac{\hbar\omega}{m_e c^2}$. The coordinates are adapted to the field direction such that $x = (x_1, x_2, x_d)$.

Now, consider an electromagnetic wave which is linearly polarized along the x_1-direction with $\hat{x} \sim d$ and spin aligned with the incident field propagation direction such that $\hat{s} = d$. For the electric dipole, we find that the scattered field has a polarization which is parallel to that of the incident field

$$\hat{E}_p \sim \hat{E} \tag{2.57}$$

and the field scattered by the magnetic dipole is orthogonal to the incoming field's polarization state such that

$$\hat{E}_m \sim \hat{E} \times d\,. \tag{2.58}$$

This suggests that for linearly polarized waves the scattered fields from charge and magnetic components will become orthogonal and, as a result, will be unable to interfere. The situation is markedly different for circularly polarized waves. In this situation,the charge and magnetic contributions interfere as the polarization states are preserved in both cases.

Typically, the magnetically scattered intensity is several orders of magnitude smaller than the charge signal. However, the situation changes when resonant scattering is considered. The magnetic distribution can be recovered by taking the difference of two diffraction patterns obtained with left and right helicities. This approach serves as the basis for imaging techniques which exploit a magnetic sample's X-ray magnetic circular dichroism [47, 17, 46, 4].

2.4 Multislice propagation method

It is often useful to understand how an incident wave propagates through a 3D sample. When considering wavelengths in the extreme ultraviolet (XUV) and X-ray regimes, finite element and boundary integral methods become computationally infeasible as the number of variables can become extremely large. The multislice method [48, 49, 50] uses a simplified approach to obtain an approximation to the field. In this method, the sample's refractive index is discretized into 2D slices which are orientated along the optical axis such that each slice is at a constant z value. The field is propagated through the sample using the following procedure:

the field is transmitted through the slice using the projection approximation, then it is free-space propagated to the next slice. These two steps are repeated until the field has been propagated through the entire sample. Numerically, the field is propagated through each sample slice of thickness Δ with

$$u_{n+1} = e^{ik\Delta}\,\mathcal{F}^{-1}\{H \cdot \mathcal{F}\{t_n\, u_n\}\}\,, \tag{2.59}$$

where u_n is the field located immediately prior to the slice at $z_n = n\Delta$ and t_n is likewise the sample transmission at $z = n\Delta$ which can be related to the sample's index of refraction through (2.31). The transfer function in the paraxial approximation is given by

$$H(q) = e^{-i\pi\lambda\Delta\,|q|^2}\,, \tag{2.60}$$

where $q \in \mathbb{R}^2$, and $|q|^2 = q_1^2 + q_2^2$. A drawback of this method is that the back-scattered field is absent and is therefore only a good approximation when the sample's refractive index is close to one. The computational speed and ease of implementation has made this a useful method for electron and short-wavelength simulations [19] as well as imaging experiments [51].

3

Short-wavelength light sources

Coherent lensless imaging techniques rely on the availability of bright and coherent light sources. This chapter introduces the underlying concepts related to three classes of short-wavelength sources. These processes depend on both quantum (single electron/atom) and macroscopic effects. The sources are capable of producing coherent bright pulses of XUV radiation making them well-suited for studying samples on the nanoscale. HHG and undulator-based sources can contain higher-order harmonics which must be accounted for using either experimental or numerical approaches. Detailed treatments of these topics are provided by [52, 34, 53, 54, 55, 56].

3.1 High-harmonic generation

In Paper I, HHG radiation was produced by focusing a high-intensity infrared laser into a cell filled with argon gas [57]. The generation process of high-order harmonics has been described using a three-step model [58, 59] which consists of: ionization, propagation, and recombination. The processes involved in this model are depicted in Fig. 3.1. The full quantum description has been described in [52]. In the ionization step, the laser's electric field distorts the atomic potential allowing an electron to tunnel into the continuum. Depending on the phase of the electric field when ionization occurs, the electron can either be driven back into the vicinity of the parent ion or out into free space. If the electron is driven back then it can recombine with the ion and emit a photon. The maximum photon energy corresponds to the ionization potential, I_p, plus the kinetic energy gained by the electron during propagation. In terms of the ponderomotive energy of the electron, U_p, the maximum

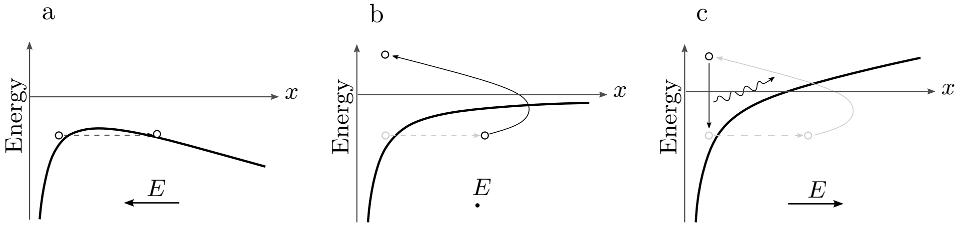

Figure 3.1: Three-step model description of the HHG process. (a) Ionization occurs when the electron tunnels into the continuum. (b) The electron propagates in the laser electric field until it returns to the atom where it (c) recombines with the atom emitting a photon.

photon energy is approximately:

$$\epsilon_{\max} \sim I_p + 3.2\,U_p\,, \tag{3.1}$$

where

$$U_p = \frac{e^2E^2}{4m_e\omega^2}\,. \tag{3.2}$$

If the laser field is elliptically polarized then the electron will likely not return, thereby preventing the HHG process from occurring. However, the broadening of the electron's wavefunction during propagation allows for recombination to occur for small ellipticity values. To obtain circular polarization one can use reflective optics after generation [60] or by using bi-chromatic driving fields [61, 62, 63, 64].

For the coherent emission of XUV photons the phase velocities of the fundamental and its harmonics should match. This leads to phase matching conditions which depend on the electron trajectory (dipole), focusing geometry (Gouy phase) and dispersion from the neutral and plasma species. These conditions can be controlled through the gas pressure, focusing geometry and laser intensity. In addition, the reabsorption of XUV photons places limitations on the length of the gain medium (gas cell). The ability of these sources to create ultrafast (femtosecond and attosecond range) pulses have made these sources indispensable for studying atomic physics involving ultrafast dynamics. A characteristic HHG spectrum filtered through an Al thin film is shown in Fig. 5.3. Here, the lower-order harmonics were removed with an Al thin film filter. The presence of multiple harmonics within the spectrum can lead to complications for coherent imaging experiments. In Chapter 5, numerical methods are described for dealing with this issue. Experimentally, a single harmonic could be selected using multi-layer mirrors or diffraction gratings [4].

3.2 Lasers

Short-wavelength lasers utilize highly ionized plasmas to create coherent radiation. The plasmas are typically created by focusing an infrared or visible laser pulse onto a particular target material or with fast electrical discharges [65]. In the hot plasma, energetic collisions strip the high-level electrons from the atom causing a population inversion resulting in single-pass, high-gain lasers. The spatial coherence must be controlled through the target geometry. These sources are capable of producing nanosecond to picosecond laser pulses with wavelengths around several nanometers [66]. Unlike HHG and undulator-based sources which contain higher-order harmonics, these sources tend to be highly monochromatic making them well suited for coherent imaging experiments. The laser which was used for CDI in Paper V used a molybdenum target in grazing incidence pump geometry to create a laser pulse with a 18.9 nm wavelength.

3.3 Synchrotron radiation

Synchrotron radiation is the light produced by a relativistic charged particle when a force has caused it to be accelerated. Synchrotron radiation is typically produced in large-scale facilities such as synchrotrons or free electron lasers. These facilities use the magnetic fields produced by bending magnets, undulators or wigglers to accelerate electrons as they pass through. In this thesis undulators were used to produce the radiation for the coherent imaging experiments and, as a result, we will discuss only these devices.

An undulator consists of two or more periodic arrays of magnets with alternating polarities. The light produced by an undulator is created when an electron bunch, traveling at relativistic speeds, gets accelerated by the alternating magnetic field. The accelerated electrons emit light and, because of their relativistic speed, the radiation is directed into a cone with a small angular opening tangential to the electron velocity. The basic principle of an undulator is illustrated in Fig. 3.2. The

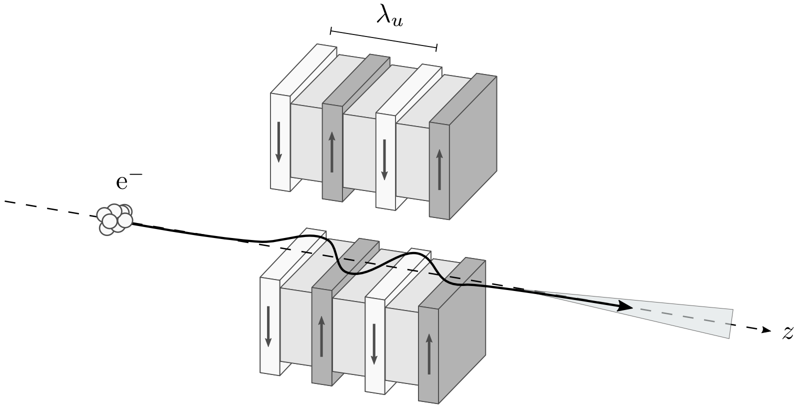

Figure 3.2: Illustration of an undulator device which produces radiation when an electron bunch – traveling at relativistic speeds – becomes accelerated by the periodic magnetic field. The photon energy can be tuned by varying the gap between the magnet arrays.

wavelength of the radiation can be tuned by changing the gap distance between the two arrays of magnets. The wavelength, λ_n, of the n$^{\text{th}}$ harmonic is given by

$$\lambda_n = \frac{\lambda_u}{2\gamma^2 n}\left(1 + \frac{K^2}{2} + \gamma^2\theta^2\right) , \tag{3.3}$$

where λ_u the undulator period, θ is the observation angle, $\gamma = 1/\sqrt{1 - v^2/c^2}$ and the dimensionless undulator parameter is

$$K = \frac{eB_0\lambda_u}{2\pi m_e c} , \tag{3.4}$$

where B_0 and m_e denote the magnetic field strength and electron mass, respectively. The undulator parameter describes the particle's oscillation amplitude relative to the undulator period. An undulator induces small oscillations ($K \ll 1$) within the electron resulting in a narrow beam of radiation, while wigglers produce larger oscillations and a wider cone of radiation. In addition, higher K values lead to more prominent higher-order harmonics which, similar to data acquired with HHG sources, introduces artifacts into the phase retrieval reconstruction (see Fig. 5.8(b))). In contrast to HHG spectra, only the first few harmonics have significant power for an undulator. This means that neighboring harmonics have large spectral separations making it easier for single harmonics to be isolated.

Specially designed undulators consisting of four arrays of magnets which can be translated relative to one another allow for the polarization state to be controlled. An important case occurs when the electrons travel along helical trajectories resulting in the production of circularly-polarized light. For non-magnetic samples with dimensions much larger than the wavelength, a single component of the electric field can be treated and we can ignore this effect. However, for magnetic samples, the polarization has a significant impact on the diffraction measurements [45]. For the most part, with exception to Section 5.3, the polarization state will be neglected and scalar diffraction theory will be utilized.

4

Coherent lensless imaging

Coherent lensless imaging techniques replace the optics found within conventional microscopes with numerical algorithms. These methods become attractive when high-quality optics are difficult to fabricate. The difficult arises for short-wavelength light as nanoscale fabrication tolerances become necessary. In the XUV region of the spectrum, the high-absorption exhibited by most materials often leads to optics with lower efficiencies. The opposite situation occurs in the X-ray spectrum where light interacts so weakly with materials that it becomes difficult to manipulate.

The theory behind two coherent lensless imaging techniques, FTH and CDI, are introduced in this chapter. The geometries associated with each one are shown in Fig. 4.1. Initially, X-ray FTH used the focus from a Fresnel zone plate as the reference wave [16]. This approach has been largely replaced by the mask-based FTH technique in which a small reference pinhole, fabricated into the sample mask, acts as the reference. This ensures that the reference and sample are mechanically stable which prevents sample vibrations from affecting the diffraction measurements. The pinhole creates a reference wave which encodes the phase into the measured diffraction pattern. The reference wave allows for the direct recovery of the sample image through the application of an inverse Fourier transform to the data. The geometry associated with a CDI experiment is even more simplified; it consists of a spatially localized (small) sample and a detector usually placed in the far-field. In theory, the spatial resolution is wavelength limited, but this comes at the expense of more complicated iterative reconstruction procedures.

An effective approach is to combine both techniques by recovering an initial reconstruction using FTH followed by phase retrieval to improve the spatial resolution [67, 4]. Several variants of FTH include multiple reference holes [68, 69, 67], extended and custom references [70, 71, 72] and uniformly redundant arrays [73]. Like-

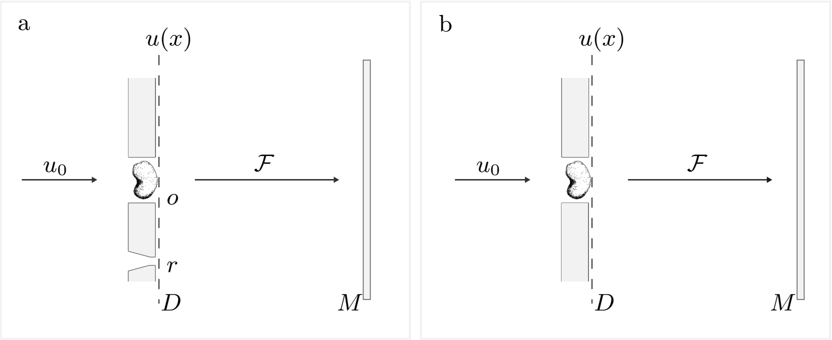

Figure 4.1: Geometries (not to scale) associated with (a) FTH and (b) CDI experiments. The sample is illuminated from the left with a coherent wave, u_0, and the diffraction pattern intensities are measured in the far-field. The far field is proportional to the ESW through the Fourier transform operator, $\mathcal{F}$. The FTH sample mask contains a reference hole which is used to encode the phase into the measured diffraction pattern.

wise, different schemes exist for CDI as well which include: ptychography [11, 12], Fresnel CDI [5] and Bragg CDI [6, 9, 10] to name a few. Overviews of these techniques are covered in [27, 30]. Many of the concepts in this chapter are related to Fourier optics which are covered in greater detail in [35].

4.1 Fourier transform holography

In an FTH experiment, the ESW emerging from the sample consists of an object wave, $o(x)$, and some known reference wave, $r(x)$, such that

$$u(x) = o(x) + r(x)\,. \tag{4.1}$$

When the incident field is monochromatic and coherent, the far-field intensity measured by the detector is given by

$$I(y) = |\hat{o}(y) + \hat{r}(y)|^2\,, \tag{4.2}$$

where $\hat{u}$ indicates the field which has been propagated into the far-field (Section 2.2.3). The data is reconstructed by applying an inverse Fourier transform to $I(y)$. Applying the Fourier convolution theorem,

$$\mathcal{F}\{f(x)\,g(x)\} = \tilde{f}(q) * \tilde{g}(q)\,, \tag{4.3}$$

we find the autocorrelation function in real-space becomes[1]

$$\begin{aligned} a(x) &= \mathcal{F}^{-1}\{I(y)\} \\ &\propto o^*(-x) * o(x) + r^*(-x) * r(x) + o^*(-x) * r(x) + o(x) * r^*(-x)\,. \end{aligned} \tag{4.4}$$

---

[1] In fact, it is actually $a \circ \varphi^{-1}(x)$ which inconsequentially is redefined as $a(x)$. Concepts related to these subtleties are described in detail in Chapter 5.

Above, $o^*(x)$ denotes the complex conjugation of $o(x)$ and $*$ is the 2D convolution operator[2]. When $r(x)$ is sufficiently separated[3] from the object, then the last two terms become separated from the first two in (4.4). In the ideal case, when $r(x) = \delta(x)$, the last two terms become the object wave and its complex conjugate. We can see two important properties of the reconstruction which stem from (4.4): first, the resolution is determined by the size of $r(x)$ and second, the reconstruction has an amplitude which is linearly proportional to $r(x)$. As the resolution scales with the reference size, it is tempting to make the reference as small as possible, but the transmission through the reference aperture will also decrease which effectively reduces the SNR in the reconstruction. Methods which were mentioned at the beginning of this chapter have been devised to circumvent this trade-off by using references with different shapes.

A simulation of an FTH experiment will be used to illustrate a few important concepts. The results of this simulation are shown in Fig. 4.2. In this simulation, a binary square is used as the sample wave and a reference hole is placed to its right. The image in Fig. 4.2(a) shows the square aperture with the spatially separated reference wave to its right. The reference wave was calculated by propagating a plane-wave through a 3D aperture until it reached the sample plane[4]. The far-

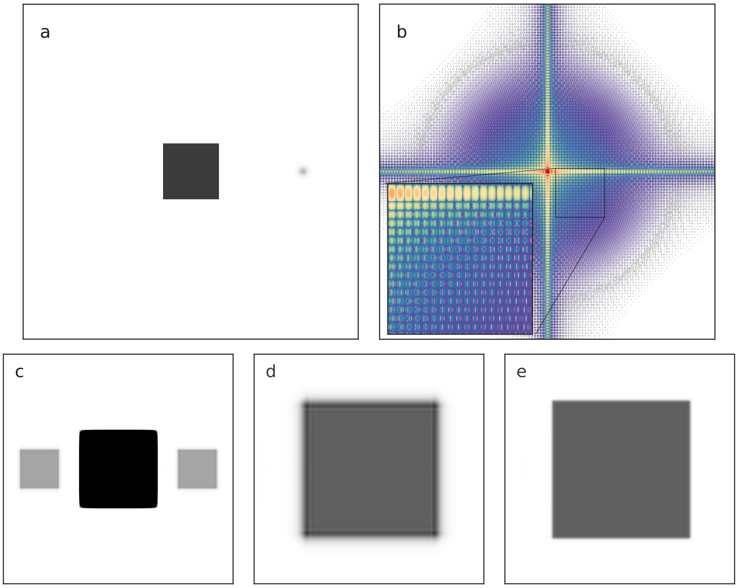

Figure 4.2: (a) Sample ESW consisting of a square sample and the (propagated) reference wave. (b) The far-field hologram intensity in log-scale. (c) The autocorrelation function results from the application of an inverse Fourier transform to the data in (b). The highest intensities (in the center) are truncated to show the reconstructions. (d) The reconstruction obtained by taking the inverse Fourier transform of the data. (e) The reconstruction from (d) propagated $1.5\mu m$ along the z-direction until it reaches the reference plane.

---

[2] The convolution operator is given by $(f * g)(x) = \int_{\mathbb{R}^n} f(y)\, g(x-y)\, dy$, where $x, y \in \mathbb{R}^n$.

[3] Roughly speaking, the separation criterion in this situation is that the reference is located a distance of at least 1.5 × object diameter from the center of the object.

[4] More discussion on this is provided in Section 4.3.

field diffraction pattern, $I(y)$, is shown in Fig. 4.2(b). The autocorrelation function is shown in Fig. 4.2(c) showing the reconstruction and its complex conjugate on either side of the signal in the center. So far, the location of $r(x)$ in relation to $o(x)$ along the propagation direction (z-axis) has not been discussed. If the separation between the sample and reference is non-zero then a reconstruction in the wrong plane will be obtained and, as a result, it will appear out of focus. To refocus the reconstruction, it must be free-space propagated into the reference plane. The initial and refocused reconstructions are shown in Fig. 4.2(d,e). These images illustrate how the refocusing procedure can improve the resolution and reduce fringe artifacts within the reconstruction. A more thorough discussion of these effects is given in Section 4.3.

4.1.1 Missing beamstop data

Typically, the large majority of the photons pass directly through the sample resulting in large intensities along the incident direction (z-axis) which can saturate or damage the detector. To protect the detector, an opaque beamstop is often used to block the unscattered light. The presence of a beamstop means that the low-spatial frequency signal is not measured, and, if larger than the central speckle, will result in unconstrained modes which cannot be recovered [19]. Reconstructing holographic data with missing beamstop data can result in fringes or ringing artifacts. A conventional reconstruction of a magnetic sample within a circular aperture [74] is shown in Fig. 4.3(a). Here, the artifacts related to the missing low spatial frequencies are clearly visible within the reconstruction.

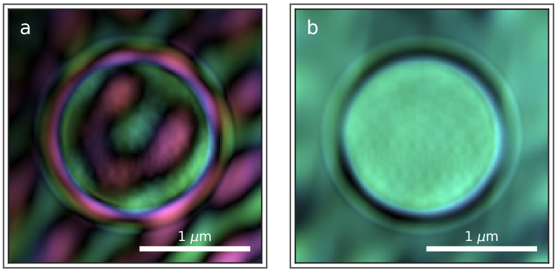

Figure 4.3: Reconstructions of a magnetic sample within a small pinhole showing artifacts due to missing data behind a beamstop. (a) Minimum energy solution obtained by applying an inverse Fourier transform to the data. (b) Minimum total variation solution obtained by solving the optimization problem described by (4.5).

By taking an inverse Fourier transform, it is implicitly assumed that the data behind the beamstop is zero; this, due to Parseval's theorem, results in the minimum energy solution. This assumption is counter to past experience and the reasoning for using a beamstop in the first place. Another approach, based on compressed sensing ideas [75, 76, 77], is to find a solution that minimizes a given cost function which simultaneously matches the measured data. In this case, the data is measured in regions of the detector where the beamstop is absent, M. This approach allows the solution to obtain non-zero values in the beamstop regions. Common cost functions are the total variation and the L^1-norm of the function. The constrained total variation[5] problem can be formulated as:

$$\begin{aligned} \min_{u} \quad & \|\nabla u(x)\|_{\mathrm{L}^1(D)} \\ \text{s.t.} \quad & \hat{u}(y) = b(y) \qquad \forall y \in M\,, \end{aligned} \tag{4.5}$$

where $b(y)$ are noisy far-field measurements[6]. The solution was found using a projected gradient descent approach. The approximate gradient calculation is described in [76]. The result is shown in Fig. 4.3(b). Another approach is to construct an unconstrained problem by combining the two terms into a single cost function consisting of the total variation and data fidelity terms. This has the benefit that the solution can deviate from the data, but has the downside that an arbitrary constant must be introduced which weighs the relative importance of the two terms. It would be inaccurate to state that one solution is more "correct" than any another, but experience tells us that the intensity values should be largest at low spatial frequencies suggesting that the minimum energy solution is a poor candidate for the ESW. On the other hand, the total variation approach is only able to affect the low-spatial frequencies preventing it from creating artificially sharp edges or other high-frequency artifacts. An alternative method, used successfully for ptychography, is to use a semi-transparent beamstop providing a compromise between attenuating the unscattered light and acquiring low-frequency data [78].

Other issues can arise which depend on the experimental geometry. As the sample-detector distance becomes smaller, data is collected at higher angles making the paraxial approximation invalid. Inspecting (2.36), we can see that the observation directions should lie on a unit sphere ($\hat{x} \in \mathbb{S}^2$), while in experiment, measurements are collected by a flat detector. In this case, it becomes helpful to interpolate the data to account for this discrepancy [79, 67, 80]. Likewise, in reflection CDI, the sample and detector planes are no longer parallel which should also be accounted for by warping the data prior to running phase retrieval [81, 82, 83].

4.2 Coherent diffractive imaging

In contrast to FTH, the phase retrieval procedure for CDI experiments relies heavily on numerical algorithms. Instead of encoding the phase into the diffraction pattern, these algorithms attempt to recover the phase iteratively from the intensity measurements together with prior knowledge about the sample. The method is more computationally demanding than the FTH reconstruction procedure, but allows for more flexibility regarding the experiment geometry and potentially higher resolution reconstructions.

The geometry of a plane-wave CDI experiment is very similar to that of an FTH experiment except a reference wave is no longer required. A sketch of the geometry

---

[5] Other types of solutions can be found by simply replacing the total variation cost with another cost function.

[6] Note that the constraint can be transformed into $\tilde{u}(q) \propto b \circ \varphi^{-1}(q) \equiv b'(q)$ so we can use the discrete Fourier transform to propagate u into the far field for comparison with the measurements.

is shown in Fig. 4.1(b). It can be useful to use an FTH sample geometry and refine the reconstruction using iterative phase retrieval [67, 4]. Additionally, one can remove the opaque mask altogether leaving only the small isolated sample. Through Babinet's principle the two geometries are equivalent [34].

Again, we will consider the incident wave to be fully coherent both spatially and temporally, monochromatic and consisting of a single polarization state. With the detector placed in the far-field, the propagation of $u(x)$ to the detector domain, M, is given by (2.47) and the measured diffraction pattern is equal to:

$$I(y) = |\hat{u}(y)|^2 \,, \tag{4.6}$$

where $y \in M$ is the spatial coordinate in the measurement domain. In the following treatment, the distinction between $\tilde{u}$ and $\hat{u}$ will be neglected as it has no effect on the analysis. Now, the far-field intensity is simply proportional to the Fourier transform of the exit wave, $I \propto |\tilde{u}|^2$.

From an abstract perspective, the strategy behind iterative phase retrieval is to use prior knowledge about the solution to construct subsets within the space of solutions. Then, the functions, u, which satisfy all these known properties are considered the solutions. This is the essence of set theoretic estimation [84]. The most successful approaches are based on alternating projections schemes, which, for two or more sets, consists of projecting u in a sequential fashion between the sets until an intersection point (solution) is found. This procedure is illustrated in Fig. 4.4 for two paths which start from different initial points. When the algorithm starts at a, the method is able to find the intersection point. However, due to the non-convex nature of $\mathcal{M}$, only a local minimum is found when it begins at b.

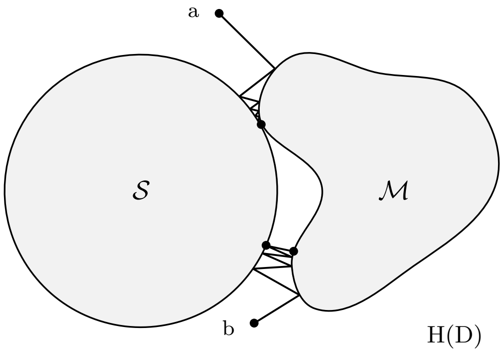

Figure 4.4: Alternating projection approach used to iteratively recover the phase from two constraint sets. The most commonly used constraints in CDI are the support, $\mathcal{S}$, and modulus, $\mathcal{M}$, sets.

Posed as a feasibility problem, the solution is given by the intersection between all constraint sets, $\mathcal{C}_i$, described by

$$\text{find} \quad u \in \bigcap_i \mathcal{C}_i \,. \tag{4.7}$$

This approach allows for information to be incorporated into the reconstruction procedure by simply increasing the number of constraint sets. The most common constraint sets for phase retrieval are determined by the sample support and the diffraction data which lead to the support, $\mathcal{S}$, and modulus, $\mathcal{M}$, sets, respectively. The feasibility problem with only these two constraints becomes

$$\text{find} \quad u \in \mathcal{S} \cap \mathcal{M}\,, \tag{4.8}$$

where the two sets are defined as

$$\mathcal{S} := \{u \in H(D) : \operatorname{supp}(u) \subseteq \Omega\} \tag{4.9}$$
$$\mathcal{M} := \{u \in H(D) : |\tilde{u}| = b\}\,. \tag{4.10}$$

In these definitions, $\Omega \subset D$ is the support domain, b are amplitude measurements, and $H(D)$ is a suitable function space in D. The support of the function u is defined as $\operatorname{supp}(u) := \{x \in D : u \neq 0\}$. Besides the support and modulus constraints, other constraints such as positivity, real-valuedness, atomicity and various types of sparsity are commonly utilized.

In experimental situations, the data is corrupted with noise which causes the intersection in (4.8) to become empty. To account for this issue, the feasibility problem can be reformulated as an optimization problem:

$$\begin{aligned} \min_u \quad & \mathcal{E}_F(u) = \|\, |\tilde{u}| - b \,\|^2_{L^2(M)} \\ \text{s.t.} \quad & \operatorname{supp}(u) \subseteq \Omega\,. \end{aligned} \tag{4.11}$$

In words, we are tasked with finding a function u, which has both, a diffraction pattern which closely matches the data, and support which is contained within Ω.

One of the most popular and simple algorithms is the error-reduction (ER) algorithm [14]. The update is given simply by

$$u^{k+1} = \Pi_S\, \Pi_M\, u^k\,, \tag{4.12}$$

where k denotes the iteration number and Π_S and Π_M are the support and modulus projections respectively. The support projection simply zeros any values of u which lie outside the support domain. Mathematically, this operation is given by

$$\Pi_S\, u^k = \begin{cases} u^k & x \in \Omega \\ 0 & x \notin \Omega \end{cases}. \tag{4.13}$$

The modulus projection replaces the amplitudes of the wave in Fourier space, $\tilde{u}$, with the measured amplitudes, while retaining the phase. This projection is specified by

$$\tilde{\Pi}_M\, \tilde{u}^k = b\, e^{i \arg(\tilde{u}^k)}, \tag{4.14}$$

which is described in real-space through the equation,

$$\Pi_M\, u^k = \mathcal{F}^{-1}\, \tilde{\Pi}_M\, \mathcal{F}\, u^k. \tag{4.15}$$

This projection simply propagates u to the measurement domain, applies $\tilde{\Pi}_M$ and propagates back to the real space domain. It was shown in [85] that the ER algorithm is equivalent to a projected gradient descent algorithm for minimizing $\mathcal{E}_F$. Also note that these projections are idempotent such that $\Pi \circ \Pi = \Pi$ which makes it easier to study the behavior of these algorithms.

As we have already noticed, the non-convexity of $\mathcal{M}$ can cause an algorithm like ER from finding the global minimum or intersection point. The hybrid input-output (HIO) algorithm has been shown to be an effective method which avoids stagnating near local minima [85]. Table 4.1 describes the HIO algorithm along with several of the most commonly used algorithms for phase retrieval including the relaxed averaged alternating reflections (RAAR) [86] and the difference map (DM) methods [87]. A combination of the ER and HIO algorithms has been shown to be an effective phase retrieval method [26] and is the approach used throughout this thesis.

Table 4.1: Update formulas of the most common phase retrieval algorithms.

Algorithm	$u^{k+1} =$
ER	$\begin{cases} \Pi_M\, u^k, & x \in \Omega \\ 0, & x \notin \Omega \end{cases}$
HIO	$\begin{cases} \Pi_M\, u^k, & x \in \Omega \\ (I - \beta \Pi_M)\, u^k, & x \notin \Omega \end{cases}$
RAAR	$\begin{cases} \Pi_M\, u^k, & x \in \Omega \\ \beta u^k + (1 - 2\beta)\Pi_M\, u^k, & x \notin \Omega \end{cases}$
DM	$\{I + \beta \Pi_S[(1+\gamma_M)\Pi_M - \gamma_M I] - \beta \Pi_M[(1+\gamma_S)\Pi_S - \gamma_S I]\}\, u^k$

4.2.1 Uniqueness

Next, we consider sampling requirements on the data which must be satisfied to recover a unique reconstruction. By uniqueness, we mean a unique equivalence class consisting of solutions which are related through translation, inversion and global phase rotation: $[u] = \{u \in H(D) : u(x) \sim u(x+a), u(x) \sim u^*(-x), u(x) \sim e^{i\alpha} u(x)\}$, where $\alpha \in \mathbb{R}$ and $a \in \mathbb{R}^2$. These ambiguities cannot be determined from the intensity measurements alone. The discussion will be based primarily on the ideas developed in [88, 89, 90, 91, 92], while homometric samples [93] will be omitted altogether.

In the discrete setting, u is typically a two or three-dimensional complex-valued array. In the two-dimensional case, $u \in \mathbb{C}^{M \times N}$, where M and N are the total number of rows and columns within the image which are often related to the number of pixels within the detector. The array can be rearranged such that u becomes a $M \cdot N$-length vector and the Fourier transform becomes a unitary matrix.

It seems reasonable, considering the work of Shannon, that a unique phase could be recovered if the intensity measurements were sampled at or above the sample's Nyquist frequency, ν_N. It turns out however, that it is necessary to sample the signal at twice this frequency. The reason for this can be seen by inspecting the intensity measurements in the real-space domain. Applying an inverse Fourier transform to the measured intensities, $\mathcal{F}^{-1}\, I(y)$, we arrive at the autocorrelation function, $a(x) = u(x) * u^*(-x)$. For a rectangular sample, $a(x)$ is twice as large as u in each direction which results in twice the Nyquist frequency. This suggests that the data must be sampled at at least $2\nu_N$. The ratio between the sampling frequency, ν_S, and ν_N is known as the oversampling ratio [94] which is defined as

$$\sigma = \frac{\nu_S}{\nu_N}\,. \tag{4.16}$$

Then, a necessary condition for uniqueness becomes

$$\sigma \geq 2 \tag{4.17}$$

in every direction. However, higher σ values do not necessarily mean the solution will be easier to find or more overdetermined. In fact, sampling the data above this value is equivalent to sampling $a(x)$ above its Nyquist frequency; we obtain no new information from these additional measurements. However, if the measurements are corrupted with noise or missing data, then finer sampling of the data may be useful by providing redundant information.

An important measure of how overdetermined the phase retrieval problem is given by the constraint ratio [92]. This quantity measures the number of independent constraints relative to the number of unknowns through the ratio:

$$\begin{aligned}\Sigma &:= \frac{\text{Number of independent autocorrelation coefficients}}{\text{Number of independent object coefficients}} \qquad (4.18)\\ &= \frac{|A|}{2|\Omega|}\,, \qquad (4.19)\end{aligned}$$

where $|A|$ and $|\Omega|$ are the size of the autocorrelation support, A, and the support, Ω, respectively. The fact that the autocorrelation function is centro-symmetric means that only half the autocorrelation coefficients are independent which gives rise to the factor of two in the denominator. A necessary condition for uniqueness is then

$$\Sigma > 1\,. \tag{4.20}$$

When $\Sigma \leq 1$, the problem is underdetermined and we cannot expect to find a unique solution without additional information. Higher values suggest that the problem is easier to solve and the solution is more likely to be unique. Several supports and their constraint ratios are shown in Fig. 4.5. We can see that Σ can be increased significantly by using a triangular support or a support which is multiply connected. In addition to having the lowest Σ values, the rectangular and disc-shaped supports are also centro-symmetric which means that they cannot differentiate between $u(x)$ and $u^*(-x)$ and can cause the algorithm to stagnate with a superposition of both solutions [95]. As a consequence, it is usually a poor

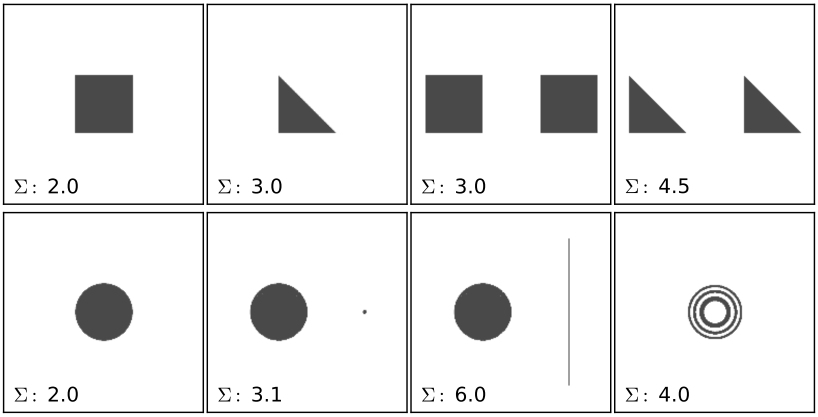

Figure 4.5: Common sample supports and their corresponding constraint ratios. Higher Σ values correspond to a higher degree of uniqueness which tend to be easier to phase.

choice to use a support which is convex and centro-symmetric. For monochromatic phase retrieval, all the geometries fulfill the requirement set by (4.20), but these values play an even more important role when considering multi-wavelength phase retrieval. More discussion of these issues is provided in Chapter 5.

4.2.2 Dynamic support and solution selection

Often it happens that either Ω is completely unknown or there is some uncertainty regarding its shape. When this happens, Ω can be treated as a dynamic variable and recovered alongside the phase using a simple approach [96]. Although there exist several variants, it is commonly calculated by thresholding the convolution between a normal distribution and $|u^k|$, such that the new support becomes

$$\Omega^{k+1} = \{x \in D : \; n_\sigma * |u^k| > t\}\,, \tag{4.21}$$

where t is a threshold value and n_σ denotes the normal distribution with standard deviation σ. A useful variant of this fixes the support size and selects the regions with the largest values as the new support. These methods are heuristic in nature and typically require monitoring the cost function or prior knowledge of the support from other means (SEM or low-resolution optical images typically). Often times it is possible to fabricate a reference hole within the sample mask allowing for a fast FTH reconstruction to be calculated and used as input into a phase retrieval algorithm.

Typically, for data which has been corrupted with noise, as the support becomes smaller $\mathcal{E}_F$ will tend to increase. Intuitively, this occurs because larger supports allow u^k to fit the high-frequency noise more closely. As a result, it can become difficult to determine the “best” solution using only $\mathcal{E}_F$ as the measure. This issue can be circumvented by viewing phase retrieval with unknown support as a multi-objective optimization problem. In this context, we would like to simultaneously minimize $\mathcal{E}_F$ and the support size, $|\Omega|$. Now, the multi-objective cost function becomes

$$\mathcal{E} = (\mathcal{E}_F,\, |\Omega|)\,. \tag{4.22}$$

Solutions which are non-dominated by any other solution constitute the Pareto front and are considered the set of acceptable solutions. These solutions are used as input to find new generations of solutions using a guided approach similar to the approach described in [97]. This allows the simultaneous usage of the shrinkwrap method and a guided approach to find an optimal solution.

Figure 4.6(a) shows a diffraction pattern taken from a puzzlepiece aperture (inset) using 500 eV X-rays. The final reconstruction and the cost values after 2250 iterations are shown in Fig. 4.6(b,c) respectively. The cost values associated with solutions which comprise the Pareto front are indicated by the red markers. The normalized Fourier error shown in Fig. 4.6(c) corresponds to: $e_F(u) = \|\,|\tilde{u}| - b\,\|_{L^2(M)} / \|b\|_{L^2(M)}$.

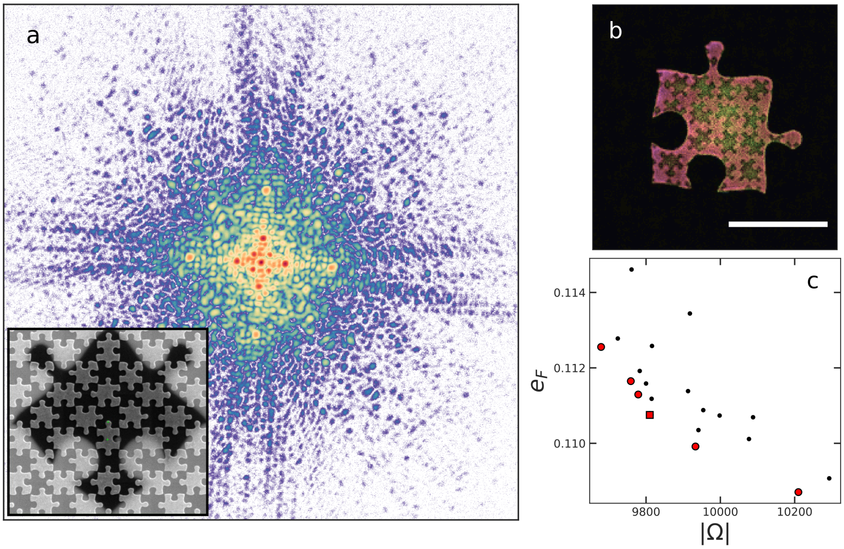

Figure 4.6: (a) Diffraction pattern (log scale) with an SEM image of the sample in the inset. (b) Reconstruction selected from the set of Pareto solutions. The scalebar corresponds to $4\,\mu\mathrm{m}$. (c) The Fourier error and support sizes for 20 reconstructions after 2250 iterations of $\mathrm{ER}_{50}\mathrm{HIO}_{100}$. The red markers correspond to the Pareto front reconstructions, while the red square corresponds to the "best" solution.

At this point, we would like to condense the Pareto set of solutions down to a single solution. Consider two cost vectors, $e^{(1)}, e^{(2)} \in \mathbb{R}^2_+$,[7] associated with solutions u_1 and u_2. The first step is to find the direction of maximum difference $j \in \{1, 2\}$,

---

[7] Explicitly, the cost vector of u_1 is: $e^{(1)} = (e^{(1)}_1,\, e^{(1)}_2) \equiv (e^{(1)}_F,\, |\Omega^{(1)}|)$.

which is determined with the formula:

$$j = \arg\max_i \frac{|e_i^{(1)} - e_i^{(2)}|}{\max(e_i^{(1)}, e_i^{(2)})} \,. \tag{4.23}$$

If $e_j^{(1)} < e_j^{(2)}$, then u_1 is considered the better of the two solutions and vice versa. This procedure can be used to sort the Pareto solutions to determine the "best" one, or, select parent solutions which can be used to create the next generation of solutions. The red square in Fig. 4.6 indicates the "best" solution according to this sorting procedure. When Ω is fixed, e_F becomes the only measure that can be used for comparisons and this method becomes equal to other guided approaches. Similar to choosing the amount of regularization in an inverse problem, there appears to be no way of avoiding heuristics when the support is an unknown dynamic variable. However, in Chapter 6 an algorithm is described which doesn't use a support constraint and therefore circumvents this issue altogether.

4.3 Thick samples and references

Up to this point we have only considered optically thin samples which allowed us to neglect any effects related to the the sample's depth. Next, we will discuss imaging thick samples with CDI and effects related to using thick references in FTH experiments.

When imaging a thick sample with CDI, the question arises as to which plane is actually reconstructed by the numerical procedure. It was shown in [98] that the support shape determines the location of this plane. In that work, a sample was considered which consisted of two planes separated by some distance along the optical axis. The samples in each plane were also separated in the transverse direction to prevent any overlap of the reconstructions. The reconstruction plane was selected by using a tight support which fits only one plane and is simultaneously loose for the other plane. The unfocused plane can be brought into focus by free-space propagating the reconstruction into this plane. Propagating the reconstruction is a common technique used in coherent lensless imaging experiments to obtain depth information about the sample and is the basis for many 3D particle tracking methods. It should be stressed that the information content within a single diffraction pattern is still 2D in nature and lies on the Ewald sphere[8]. An overview of these concepts and on tomography in general is given in [39]. A comparison between 2D and full 3D reconstructions and discussion on defocus artifacts can be found in [44].

In contrast, the reconstruction plane in an FTH experiment is determined by the reference wave. In Paper IV, the dependency of the resolution and location of the reconstruction plane on the 3D shape of the reference aperture was studied. These effects were studied experimentally by analyzing the far-field diffraction patterns from references with different geometries. Two SEM images showing the internal

---

[8] When the Born approximation is valid.

structure of these references are shown in Fig. 4.7. Each reference consists of a

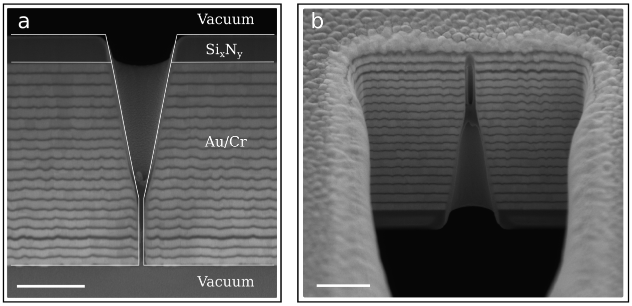

Figure 4.7: SEM views of two reference apertures with different diameters. The apertures consist of 200 nm of silicon-nitride and 1850 nm thick Au/Cr bilayers. (a,b) The references have diameters of approximately 40 nm and 70 nm respectively. The largest opening has a diameter of 500 nm for both references. The scalebars correspond to 500 nm. Figure adapted from Paper IV.

200 nm thick layer of silicon-nitride which supports a series of Au/Cr bilayers with a total thickness of 1850 nm. The Au/Cr bilayers constitute the holographic mask which ensures that the holographic separation conditions are met. These reference geometries are characteristic of references used for studying magnetic thin-films [30, 99]. In these experiments the silicon-nitride layer was used to support the magnetic thin-film. In the diffraction experiments, the X-ray photon energy was set to 780 eV and was circularly polarized. Several diffraction patterns and their recovered ESWs are shown in Fig. 4.8. The ESWs were recovered using an iterative phase retrieval procedure which was described in the previous section.

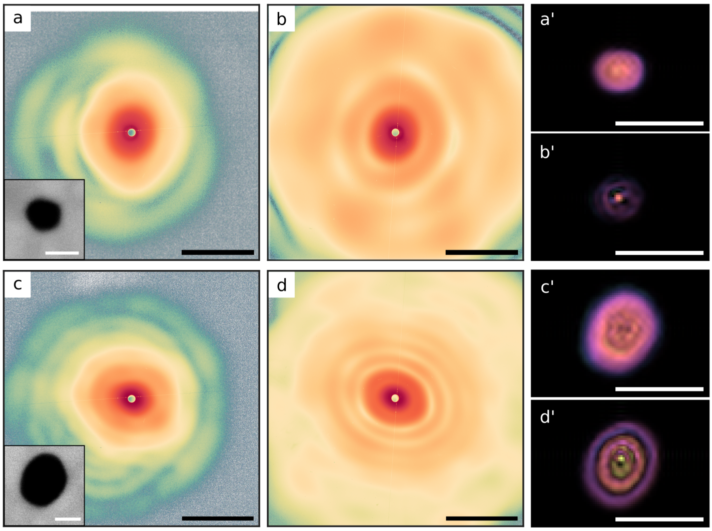

Figure 4.8: (a–d) Diffraction measurements (log-scale) from 40 nm and 100 nm diameter references when the incident field illuminates the Au (a,c) or silicon-nitride (b,d) side. The scalebars correspond to 50 µm^{-1}. The insets show SEM images of the references with 50 nm scalebars. (a'–d') Phase retrieval reconstructions corresponding to the diffraction patterns in (a–d). The scalebars indicate 100 nm. Figure adapted from Paper IV.

In addition, the multislice technique was used to simulate a plane wave propagating through the reference aperture. Multislice simulations for 70 nm references are shown in Fig. 4.9 for two configurations. In these images the plane-wave is incident from the left. The exit wave from these simulations were used as the reference wave for the simulation of FTH experiments. An ESW from one of these simulations is shown in Fig. 4.2(a) showing a binary square sample and the reference located to the right. A binary square 1 µm wide was used as the sample and placed on the outer surface of the silicon-nitride. The sample was made to be infinitely thin in order to isolate the reference effects on the reconstruction. The location of the sample plane is indicated by the red dashed lines in Fig. 4.9. The reconstruction was obtained by applying an inverse Fourier transform to the data is shown in Fig. 4.2(d) and the refocused reconstruction in Fig. 4.2(e).

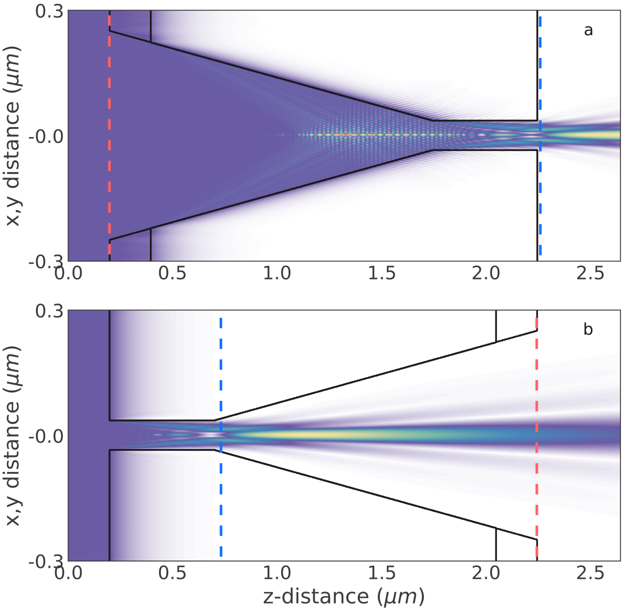

Figure 4.9: Multislice simulation results showing the field amplitude as it propagates through thick reference apertures. The plane-wave is incident from the left and the red and blue dashed lines indicate the sample and reconstruction planes respectively. The field is either incident on (a) the silicon-nitride layer or (b) the Au layer. Figure adapted from Paper IV.

The binary square was used as a sample to determine the location of the reconstruction plane as it has a very small total variation when it is in focus. Out of focus, the reconstruction contains fringes and smoother edges which result in higher total variation values. Finding the propagation distance corresponding to the smallest total variation value allowed for the location of the reconstruction plane to be precisely determined. The locations of the reconstruction planes are shown by the blue dashed lines in Fig. 4.9. The location of the reconstruction plane was nearly invariant with respect to the reference diameter which ranged from 40 nm–100 nm.

Lastly, the resolution and reconstruction plane were studied for different opening angles. The geometry and opening angle definition are shown in the inset of Fig. 4.10. We can see that as the opening angle increases the reconstruction plane transitions from the outer silicon-nitride surface to the exit of the cylindrical opening approximately 1.5 µm away. In this transition region (0°–3°) the diffracted wave interacts with the walls of the reference making it appear larger than it really is. Therefore, it is important to avoid these small-angle geometries to obtain the highest possible resolution.

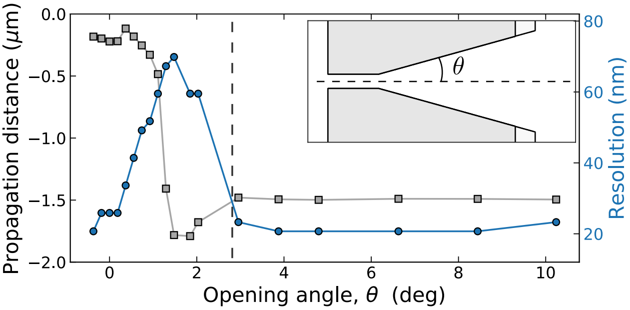

Figure 4.10: Resolution and propagation distance dependence on the aperture's opening angle. The inset shows the reference geometry used in the multislice simulations. Figure adapted from Paper IV.

5

Multi-wavelength coherent diffractive imaging

In this chapter the extension of phase retrieval to include multi-wavelength data is explored. We will consider the same experimental geometry (Fig. 5.1) as that of monochromatic CDI except now the source spectrum consists of several wavelengths. For HHG and undulator-based sources, these wavelengths may originate from the distinct higher-order harmonics which are inherently present [100] or by employing multiple undulators with different gap separations [101, 102, 103]. Unlike ptychography, which uses the redundant information within the measurements to recover additional information [104, 105, 106, 51], in a CDI experiment one has access to only a single diffraction image. Previous experiments have shown that phase retrieval can be applied when the source is partially coherent [107, 108, 109, 110, 111, 112, 113, 114]. In these experiments, the beamline efficiency can be improved by lowering the amount of spectral filtering which is necessary. Among the CDI methods capable of singleshot imaging, the algorithms require that the exit waves are the same for all wavelengths up to a multiplicative factor. As a result, they do not provide additional information with respect to monochromatic CDI experiments. In the XUV regime, this transmission constraint requires a binary sample transmission. In this chapter, algorithms are described to extend phase retrieval beyond its current status by performing source separation and phase retrieval simultaneously. This has applications for imaging when the data consists of an incoherent superposition of intensities which can occur when the source is comprised of multiple wavelengths or polarization states.

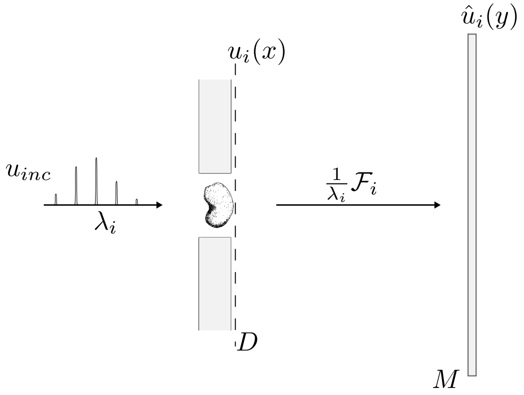

Figure 5.1: Illustration showing the geometry of a multi-wavelength CDI experiment. The source spectrum now consists of several distinct wavelengths which each contribute to the diffraction pattern.

5.1 Partial coherence

The partial coherence properties of the incident wave has a significant effect on the measured diffraction pattern, and, as a result, changes to the data treatment procedure and phase retrieval algorithms are necessary. The relevant theory of partially coherent fields is introduced in this section to gain insight into diffraction data obtained with a multi-wavelength source. This knowledge will be used in the next section to develop multi-wavelength phase retrieval algorithms. Comprehensive treatments regarding partial coherence effects can be found in [115, 116, 28, 36].

Next, the cross-spectral density, W, will be used to calculate an expression for the total intensity, I, measured by the detector. The cross-spectral density is given by

$$W(x_1, x_2, \omega) = \int_{\mathbb{R}_+} \langle U(x_1, \omega) \cdot U^*(x_2, \omega') \rangle \, d\omega' \,, \tag{5.1}$$

where U is a random vector field and $\langle \cdot \rangle$ denotes an ensemble average. Throughout this chapter, we will consider fields that are comprised of several, distinct frequency components of the form

$$U(x, \omega) = \sum_{i=1}^{P} U_i(x) \delta(\omega - \omega_i) \,, \tag{5.2}$$

where i is a wavelength index and P is the number of wavelengths. In (5.2) we have neglected the finite width of each frequency component, but we will see later that this model agrees well with double-slit measurements from a HHG source. Inserting (5.2) into (5.1) we obtain

$$W(x_1, x_2, \omega) = \sum_{ij} \langle U_i(x_1) \cdot U_j^*(x_2) \rangle \, \delta(\omega - \omega_i) \,, \tag{5.3}$$

To simplify the calculation, we will consider fields which have full spatial coherence. Discussions related to CDI with fields which exhibit partial spatial coherence can be found in [114, 117, 112, 113]. In addition, we neglect interference from cross terms ($i \neq j$) as detector integration times are often large compared to the beat frequencies. The intensity measured by the detector is given by

$$I(y) = \int_{\mathbb{R}_+} W(y, y, \omega) d\omega \,. \tag{5.4}$$

Then propagating (5.3) into the far field we find the intensity measured by the detector is given by an incoherent sum of intensities

$$I(y) = \sum_{i=1}^{P} \hat{u}_i(y) \cdot \hat{u}_i^*(y) \tag{5.5}$$

$$= \sum_{i=1}^{P} I_i(y) \,. \tag{5.6}$$

The contribution from each frequency component to the total intensity is described by the spectral intensities

$$S_i := \frac{\int_{\mathbb{R}^2} I_i(x) dx}{\int_{\mathbb{R}^2} I(x) dx} \,. \tag{5.7}$$

Inspecting equations (5.5) and (5.6), we can see that the total intensity is comprised of a incoherent sum from each frequency and polarization component[1]. For large,[2] non-magnetic samples, the polarization of the scattered field will coincide with that of the incident field. This allows us to use scalar diffraction theory and treat u as a scalar function by considering each component of the vector field separately. At the end of this chapter we will look at the application of CDI to magnetic samples. For these samples, the polarization of the field is affected and the detector measures in an incoherent sum associated with two polarization states.

We are concerned with the relative scaling of each field with respect to one another or relative to some reference wave, u_0. We make this explicit by rescaling u_0 such that $\hat{u}_0 \to \tilde{u}_0$ and $y \to \frac{y}{\lambda_0 z}$ in (2.47). The transformation becomes $\varphi_i(y) = \frac{\lambda_i}{\lambda_0} y$ and the far field is related to the Fourier transform, $\tilde{u}_i$, through

$$\hat{u}_i = \frac{\lambda_0}{\lambda_i} \, \tilde{u}_i \circ \varphi_i^{-1} \tag{5.8}$$

and after applying an inverse Fourier transform we find[3]

$$\check{u}_i := \mathcal{F}^{-1} \, \hat{u}_i \tag{5.9}$$

$$= \frac{\lambda_i}{\lambda_0} \, u_i \circ \varphi_i \tag{5.10}$$

---

[1] Stemming from the dot product.

[2] Compared to λ_i.

[3] Using the identity: $\mathcal{F}\{u(ax_1, ax_2)\} = \frac{1}{a^2} \, \tilde{u} \left(\frac{q_1}{a}, \frac{q_2}{a} \right)$, where $a \in \mathbb{R}$.

It is important to notice that the size of $\check{u}_i$ depends on λ_i through φ_i; this observation is key to the success of the multi-wavelength phase retrieval algorithm described in Paper II and in the next section.

Now we are in a position to analyze the autocorrelation function from a multi-wavelength double-slit diffraction pattern. For a double-slit sample, the ESWs are all proportional and given by $u_i(x) = \sqrt{S_i}\,(s(x) + r(x))$, where $s(x)$ and $r(x)$ are functions describing each rectangular slit[4]. The measured intensity is then proportional to

$$I(y) \propto \sum_i S_i |\hat{s}_i(y) + \hat{r}_i(y)|^2 \,. \tag{5.11}$$

Applying an inverse Fourier transform to (5.11), we find that the autocorrelation function is proportional to

$$\begin{aligned} a(x) \propto \sum_{i=1}^{P} S_i[&\check{s}_i(x) * \check{s}_i^*(-x) + \check{r}_i(x) * \check{r}_i^*(-x) \\ &+ \check{s}_i^*(-x) * \check{r}_i(x) + \check{s}_i(x) * \check{r}_i^*(-x)] \,. \end{aligned} \tag{5.12}$$

The last two terms have a spatial separation from the center of $a(x)$ which is dependent on λ_i. This produces the multiple horizontal lines which can be seen in Fig. 5.2. This figure shows a multi-wavelength autocorrelation function associated with a double-slit sample. The S_i values can be read off directly from $a(x)$ by measuring the relative peak intensities from each $\check{s}_i(x) * \check{r}_i^*(-x)$ term; this can be accomplished by plotting the signal along the vertical dashed line in Fig. 5.2[5]. The wavelength associated with each line can be determined by measuring the distance from the center to the i$^{\text{th}}$ horizontal line using the relation

$$\lambda_i = \frac{\Delta_d N d}{n_i z} \,, \tag{5.13}$$

where n_i is the number of pixels from the center to the i$^{\text{th}}$ line and d is the slit separation. A description of this approach using a quasi-monochromatic approximation is given in [118, 119]. A comparison between an extracted spectrum and one obtained with a flat-field XUV spectrometer is shown in Fig. 5.3. The two spectra are measured at different locations in the beamline. The calculated reflectivity of two multilayer mirrors is applied to the XUV spectrum (black line) to obtain the expected spectrum (red line) located at the location of the double-slit. The double-slit diffraction data and their corresponding fits using the extracted spectrum are shown in Fig. 5.4. It is apparent that the calculated lines match the data closely suggesting that our model accurately describes the situation.

---

[4] The two functions can be related through a simple translation such that $s(x) = r(x - a)$.

[5] It turns out the convolution and function composition operations end up canceling the $(\lambda_i/\lambda_0)^2$ factor to make the maxima of each line equal to S_i.

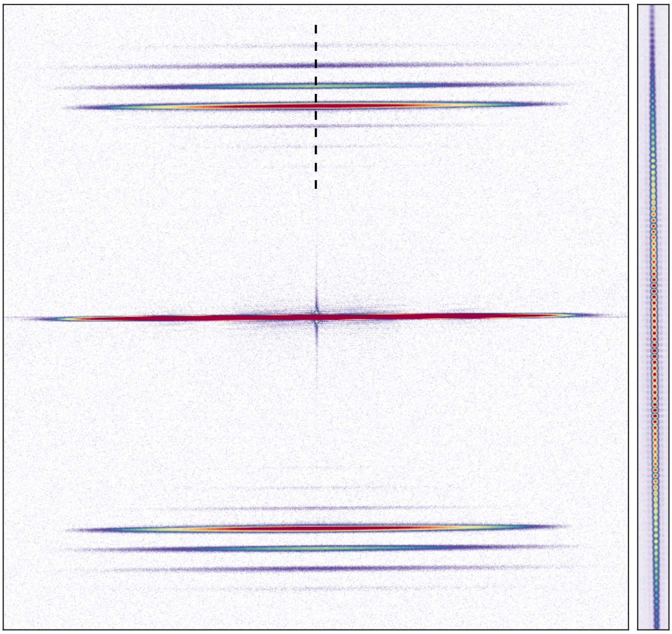

Figure 5.2: Autocorrelation function from a double-slit diffraction pattern which was taken with an HHG source. The highest intensities were truncated to show the lower intensity values more clearly. The center section of the diffraction pattern is shown on the right.

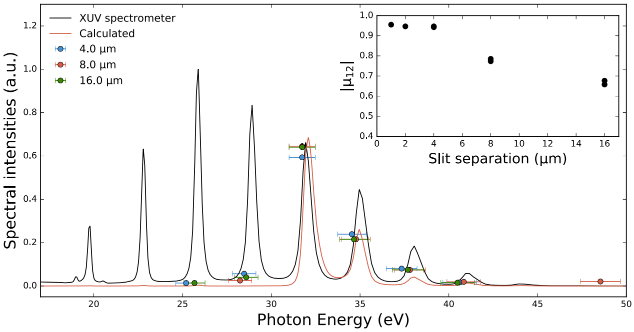

Figure 5.3: The extracted spectrum using the autocorrelation function from a double-slit diffraction pattern. The inset shows the magnitude of the complex degree of coherence for different double-slit separations. Figure adapted from Paper I.

5.2 Multi-wavelength phase retrieval

If the sample transmission is independent of λ_i and the incoming fields are all proportional, then $u_i = \sqrt{S_i/S_0}\, u_0$ then from (5.8) we see that the diffracted intensities

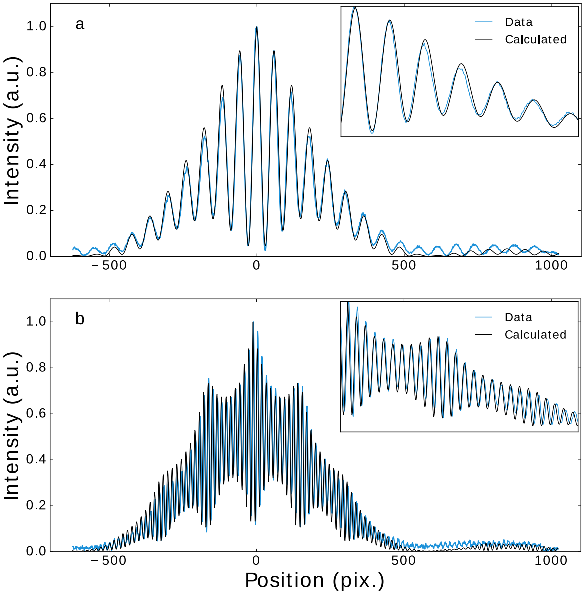

Figure 5.4: Comparisons between measured (blue) and calculated (black) diffraction patterns from double-slit samples with 2 and 8 µm slit separations. Closeups of the middle section are shown in the insets. Figure adapted from Paper I.

are related through

$$I_i(y) = \frac{S_i}{S_0}\left(\frac{\lambda_0}{\lambda_i}\right)^2 I_0 \circ \varphi_i^{-1}(y)\,, \tag{5.14}$$

where λ_0 corresponds to the reference wavelength and λ_i are ordered such that $\lambda_1 < \lambda_2 < \ldots \lambda_P$. We can use (5.14) to find a pseudo-monochromatic diffraction pattern, I_0, from the measured polychromatic data, $I_m(y)$. The cost function used for this procedure is defined as:[6]

$$\mathcal{E}(I_0) = \left\| \sum_i S_i \psi_i\{I_0\} - I_m \right\|^2_{L^2(M)} + \mathcal{E}_2(I_0)\,, \tag{5.15}$$

where $\psi_i\{I_0\}(y) = (\lambda_0/\lambda_i)^2\, I_0 \circ \varphi_i^{-1}(y)$ and $\mathcal{E}_2$ is a cost function which can be used to promote sparsity or incorporate prior knowledge.

The procedure was applied to singleshot polychromatic diffraction patterns of a puzzlepiece aperture. The S_i values are fixed when minimizing (5.15) and were extracted from a double-slit diffraction pattern. The diffraction pattern is shown in Fig. 5.5(a). The pseudo monochromatic diffraction pattern which results from minimizing the cost function in (5.15) is shown in Fig. 5.5(b). At this point, monochromatic phase retrieval algorithms can be used to find the sample image. The result of running $\mathrm{ER}_{50}\mathrm{HIO}_{100}$ on the image in Fig. 5.5(b) results in the reconstruction shown in Fig. 5.5(c). This procedure has the benefit of reducing the number of

---

[6] Note that a factor of $1/S_0$ has been absorbed into I_0 in order to stay consistent with the notation in Paper I.

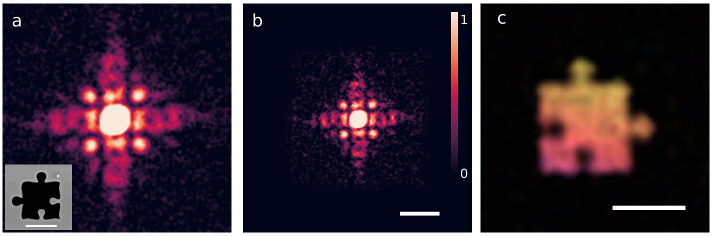

Figure 5.5: (a) A singleshot polychromatic diffraction pattern obtained from the puzzlepiece shown in the inset. (b) The extracted pseudo-monochromatic diffraction pattern. The scalebar corresponds to $1\,\mu\mathrm{m}^{-1}$. (c) Reconstruction using ER$_{50}$HIO$_{100}$. The scalebar corresponds to $4\,\mu\mathrm{m}$. Figure adapted from Paper I.

unknowns by using the relation in (5.14), but the procedure is limited to samples which have simple transmission functions. This limitation is overcome by the next algorithm by recovering each u_i separately.

Typically, a CDI sample is either small and isolated in free space, or is placed within the opening of an opaque mask (Fig. 5.1). In both cases, the sample support is the same for each λ_i, however, unlike the previous situation, we will not assume that the u_i are proportional. Instead, we exploit the scaling of the waves given by (5.10) to obtain different support constraints for each field. Equation (5.10) leads to supports which are related by

$$\Omega_i = \{x \in D : \varphi_i(x) \in \Omega_0\}\,, \tag{5.16}$$

where Ω_0 is a reference support associated with the largest S_i value and the transformation is again given by $\varphi_i(x) = \frac{\lambda_i}{\lambda_0}x$. The straightforward extension of the support projection from Section 4.2 gives

$$\Pi_S \check{u}_i(x) = \begin{cases} \check{u}_i(x) & x \in \Omega_i \\ 0 & x \notin \Omega_i \end{cases}\,. \tag{5.17}$$

Now, $\check{u}$ must be used instead of u_i because $\check{u}_i$ and $\hat{u}_i$ are a Fourier pair and we can no longer use $\tilde{u}_i$ to describe the far field. This can be accounted for at the end by inverting (5.10) to determine u_i. The effect of φ_i on the size of the reconstructions can be seen in Fig. 5.6. Each $\check{u}_i$ is normalized according to

$$\Pi_N \check{u}_i(x) = \sqrt{S_i}\,\check{u}_i(x)\,\frac{\|b\|_{L^2}}{\|\check{u}_i\|_{L^2}} \tag{5.18}$$

to ensure that the calculated total diffraction pattern has the correct spectral weightings. We must compare $\sqrt{I(y)}$ with the measured amplitudes, $b(y)$, so now the magnitude projection becomes

$$\tilde{\Pi}_M \hat{u}_i(y) = \frac{\hat{u}_i(y)}{\sqrt{I(y)} + \epsilon}\,b(y)\,, \tag{5.19}$$

where ϵ is a small positive constant to prevent issues from arising for small $I(y)$ values. This operation rescales the amplitude of each u_i which can be viewed as a projection onto a sphere, $\mathbb{S}^{2P-1}$, where P is the number of wavelengths. The monochromatic projections defined in Section 4.2 can be replaced with these generalized projections and used with the algorithms described in Table 4.1.

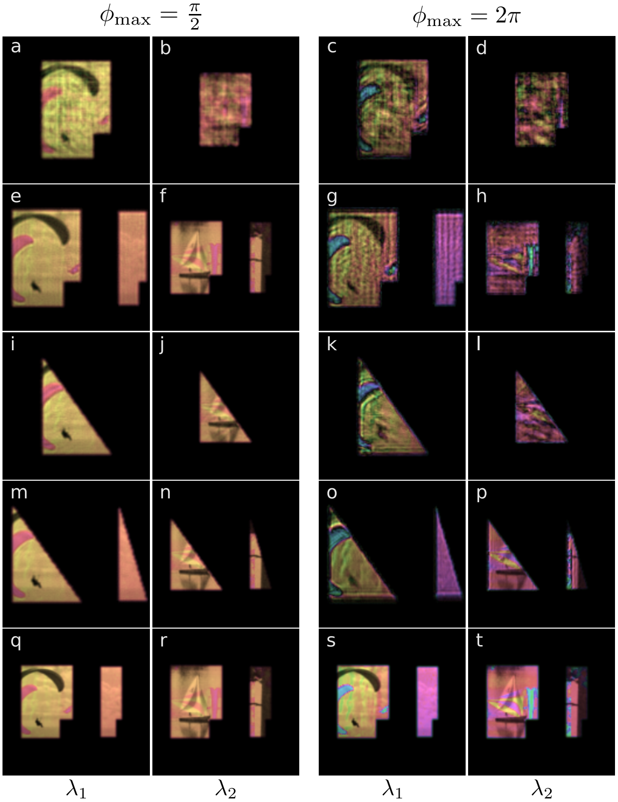

Figure 5.6: Reconstructions associated with the two wavelengths for different support shapes (rows) and different amounts of phase within the ESWs. The last row shows the true ESWs for the double rectangle support. Figure adapted from Paper II.

Before we look at the algorithm's numerical performance, we should understand when to expect a unique solution. A straightforward modification to Σ from Section 4.2.1 will allow us to account for the additional unknowns. The number of unknowns is given by the total number of unknown coefficients within Ω_i associated with each u_i. From a direct application of (4.18), we find that the polychromatic constraint ratio becomes

$$\Sigma = \frac{|A|}{2\sum_i |\Omega_i|}. \tag{5.20}$$

Now, $A = \cup_i A_i$, which corresponds to the polychromatic autocorrelation support. The polychromatic autocorrelation function is obtained by applying an inverse Fourier transform to the polychromatic intensity data. When the incident field contains two wavelengths such that $\lambda_1 \sim \lambda_2$, then Σ becomes approximately half its monochromatic value. Inspecting the monochromatic constraint ratios in Fig. 4.5, we see that the rectangular and disc-shaped supports give $\Sigma \sim 1$. This suggests that the algorithm will have difficulty finding the solution under these circumstances. The Σ values can be increased by using supports which are non-convex or multiply connected or when the λ_i values are significantly different from one another.

The method was studied numerically as a function of the source spectrum, the support geometry and the degree of complexity, $\phi_{\max}$, of the ESWs. Reconstructions, $\check{u}_i$, for two wavelengths are shown in Fig. 5.6 for different $\phi_{\max}$ values and different support shapes. The last row shows the true u_i for the double rectangle support. The double triangle support clearly shows the best reconstructions which should not be surprising since it has the largest Σ value out of the four supports. We can also see that the reconstruction quality degrades for larger $\phi_{\max}$ values.

Fig. 5.7 shows the reconstruction error for two different $\phi_{\max}$ values. The solid and dashed lines correspond to $\phi_{\max} = \pi/2$ and $\phi_{\max} = 2\pi$ respectively. This plot also shows the importance that Σ plays on the reconstruction quality. In addition, larger wavelength discrepancies lead to improved reconstruction quality. This can be explained through the following simple explanation: as λ_1/λ_2 becomes smaller the number of unknowns decrease relative to $|A|$ which leads to a higher Σ value.

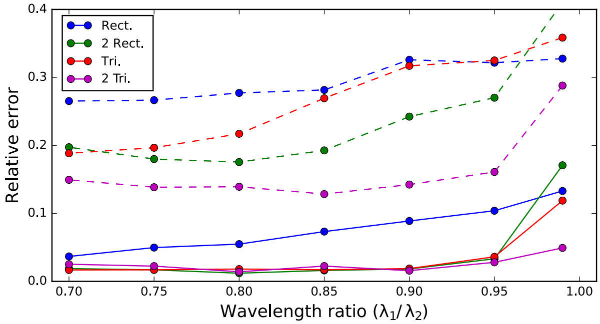

Figure 5.7: Relative error dependence on the source spectrum for four different support shapes. Each point is the average error from 20 independent trials. The solid and dashed lines correspond to maximum phase values of $\pi/2$ and 2π within the ESWs. Figure adapted from Paper II.

The method was applied to multi-harmonic synchrotron diffraction data of a commercial hard drive. The data is shown in Fig. 5.8(a) in log scale. The thinning and sample preparation procedures necessary to image the sample in transmission geometry are described in detail in [74]. The photon energy was set to the L_3 absorption edge of Co to obtain the maximum magnetic contrast. The monochromatic phase retrieval reconstruction obtained with $\mathrm{ER}_{50}\mathrm{HIO}_{100}$ is shown in Fig. 5.8(b). In comparison, the reconstructions using the multi-wavelength phase retrieval procedure are shown in Fig. 5.8(c,d) for the fundamental and second-order harmonics of the undulator. A clear improvement in the reconstruction quality is evident between the two procedures. The unconstrained modes due to missing data in the beamstop regions in the reconstructions were determined using the total variation minimization procedure described in Section 4.1.1. The reconstruction in Fig. 5.8(c) can be compared to the holographic reconstructions of the same sample shown in Fig. 4.3. The holographic reconstructions in Fig. 4.3 do not account for the higher-order harmonics which explains the presence of the non-zero background signal.

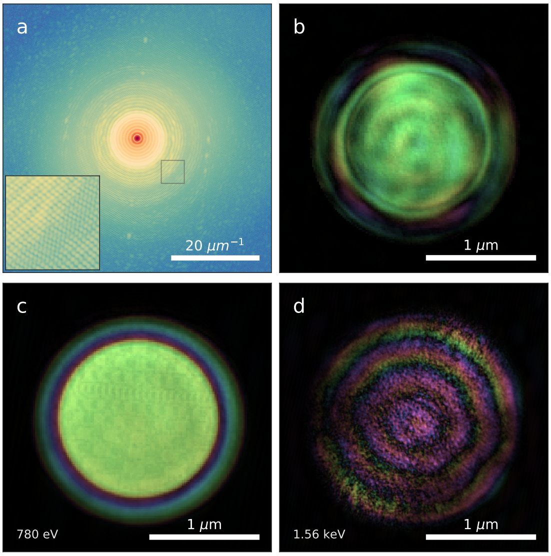

Figure 5.8: (a) Diffraction measurements (log scale) from a magnetic hard disk contained within a circular gold holographic mask. (b) Reconstruction obtained using a conventional (monochromatic) phase retrieval method. (c,d) Reconstructions associated with the first and second-order harmonics obtained with the multi-wavelength phase retrieval method.

More generally, nonlinearity within an inverse problem is typically viewed as a complication which is treated using a linearization procedure. Instead, this method suggests that nonlinearity can be exploited to solve for unknowns which would otherwise be impossible to recover[7]; an idea that was even suggested for explaining the absence of magnetic monopoles within the general theory of relativity [120].

5.3 Vector CDI for magnetic samples

In this section, we adapt the previous approach for the purpose of recovering a sample's charge and magnetic contributions from a single diffraction pattern. Consider a monochromatic, linearly-polarized (horizontal) field incident on a sample comprised of two triangular openings. The first opening is covered by a thin magnetic film and the second opening is either covered by a non-magnetic film or is open. If the scattered field can be accurately described by electric and magnetic dipole terms from Section 2.3, then, the polarization of the magnetically scattered field becomes

---

[7] Consider the counter-intuitive example where measurements of the complex field could be made directly; in this context, the forward operator would be proportional to the Fourier transform. As a result of the linearity, any linear combination of the exit waves would still fulfill the data constraint and we would no longer be able to recover each of the ESWs individually.

orthogonal (vertical) to the incident field. This results in a diffraction pattern which consists of an incoherent superposition of intensities from these two polarizations [45, 121]. Our aim is to recover the ESWs associated with these two polarizations. The primary technique used to study magnetic thin films with coherent X-rays acquires diffraction patterns from both left and right helicities and combines these measurements to find the magnetic and charge distributions [17, 30, 4]. In contrast, this method could use linearly polarized light and would require only a single diffraction pattern.

The algorithm uses two pieces of information to solve the problem: first, linearly polarized light can be decomposed into equal parts of left and right polarizations, $u_x = \frac{1}{\sqrt{2}}(u_r + u_l)$, or, $u_y = \frac{i}{\sqrt{2}}(u_r - u_l)$. Second, we know that the magnetic material covers only a single opening. This means that the support for the vertically polarized ESW will contain only a single opening while the horizontally polarized ESW will be comprised of both openings. The fact that linearly polarized light can be decomposed into equal amounts of right and left helicities is equivalent to knowing the spectral intensities in multi-wavelength phase retrieval.

In the simulation, two ESWs are created which correspond to the horizontal (charge) and vertical (magnetic) polarizations. A thin film is simulated with magnetic moments which are either parallel or anti-parallel to the propagation direction (z-axis) such that the discussion in Section 2.3 is relevant. The spatial distribution of the magnetic domains was simulated using the procedure described by [122]. The resulting horizontal, vertical and total diffraction patterns are shown in Fig. 5.9(a–c) respectively. The recovered ESWs associated with left and right helicities are shown in Fig. 5.9(d,e). The two ESWs are subtracted to obtain the vertically polarized ESW which corresponds to the sample's magnetic contribution. Similarly, adding the two we obtained the horizontal ESW associated with charge scattering. The charge and magnetic ESWs are shown in Fig. 5.9(f,g) respectively which can be compared to the exact ESWs in Fig. 5.9(h,i). The supports for the horizontal and vertical polarizations are shown in Fig. 5.9(j,k) respectively which were used to separate the two contributions.

As we can see, the algorithm is able to recover ESWs associated with both polarizations using the support diversity and the fact that linearly polarized light can be decomposed into equal parts of left and right helicities. This method should open up the possibility to study magnetic samples with linearly polarized light from single diffraction measurements which currently requires two diffraction measurements. The success of this method depends on the relative strength of the magnetic contrast and ultimately on the accuracy of the model described in Section 2.3.

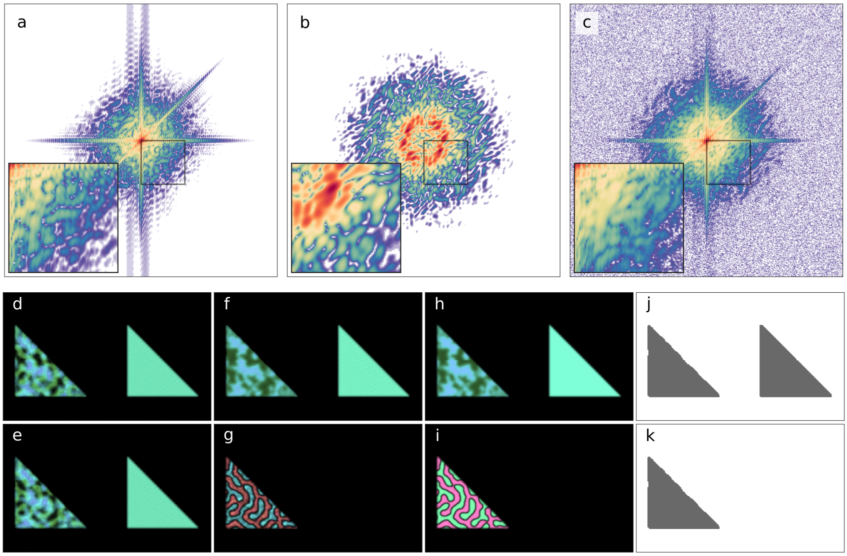

Figure 5.9: Recovery of the charge and magnetic contributions from a single diffraction pattern. The total intensity (c) is comprised of an incoherent summation of charge (a) and magnetic (b) contributions. (d,e) Reconstructions of the ESWs of the left and right helicities. (f,g) Reconstructions of the charge and magnetic distributions within the sample. (h,i) The exact ESWs associated with the charge and magnetic distributions. (j,k) The charge and magnetic supports used to separate the two contributions.

6

Image registration for phase retrieval

It is common for the sample shape to be unknown prior to the phase retrieval process. In this situation, it is possible to recover the support using heuristic approaches such as the “shrinkwrap method” described in [96]. However, this introduces a trade-off between the support size and data fidelity which resembles that between regularization and data fidelity present in many inverse problems. As the algorithm progresses and the support shrinks in size, the reconstructions are unable to account for the rapid oscillations due to noise within the measurements. This trade-off produces a difficulty when choosing the “best” estimate to be used as the final reconstruction.

In this chapter we explore a very different approach to phase retrieval which is based on ideas from non-rigid image registration and circumvents the need for a support. The method starts with an initial (template) image and attempts to find a transformation which “warps” this image until the diffraction pattern matches the data. In short, it registers the template to match the target indirectly through their diffraction patterns. The approach attempts to find large deformations using the large deformation diffeomorphic metric mapping (LDDMM) approach [123] and is motivated by previous work on image registration for solving inverse problems [124, 125]. Another way of viewing this algorithm is from the registration perspective. From this perspective, the algorithm removes the need to find an initial rigid translation between the template and target images. This is due to the fact that the diffraction amplitudes are invariant with respect to translations. An overview of registration techniques is given in [126] which describes possible deformation models, optimization procedures and matching criteria.

6.1 Registration Theory

A brief overview of the theory behind the method presented in Paper III is given in this section. The underlying concepts from differential geometry can be found in [127] and an introduction to the necessary notation is provided in Appendix A. In this method, images are treated as differential forms which allows for the concise mathematical framework of differential geometry to be utilized. The formalism has shown its utility in areas such as image registration [128] and shape optimization [129] problems.

The aim of this method is to find a diffeomorphism[1], $\varphi : D \to D$, from a smooth manifold, D, to itself which transforms our initial guess (template), α_0, such that its diffraction pattern matches the data, $b^2 = (F\alpha_1)^2 + \text{noise}$. Here, the forward operator is defined by $F\alpha_i := |\mathcal{F}\alpha_i|$ and α_1 is the unknown target. The differential forms are related to images, I_i, through $\alpha_i = I_i$ when $\alpha_i \in \Omega^0(D)$ or $\alpha_i = I_i \,\mathrm{vol}_g$ when $\alpha_i \in \Omega^n(D)$ for $i \in \{0, 1\}$. The action, $\varphi_* \alpha$, is defined as the push-forward which is related to the pull-back operation through $\varphi_* \alpha = (\varphi^{-1})^* \alpha$. The actions corresponding to $\alpha \in \Omega^0(D)$ and $\alpha \in \Omega^n(D)$ will be referred to as the geometric and mass-preserving actions respectively. Further details on differential forms and these actions can be found in Appendix A.

In realistic experiments the noise within the measurements prevents any exact matching from occurring. This means we must use a cost function which promotes the similarity between diffraction patterns. For reasons elucidated below, we will use a similarity function based on the normalized cross correlation, but for the moment, we will use the sum-squared difference as this corresponds to the original LDDMM method and is the most familiar.

The LDDMM method uses a time-dependent velocity field in the space of smooth vector fields, $v_t \in V$, to generate φ through the flow equation

$$\frac{d\phi_t^v(x)}{dt} = v_t \circ \phi_t^v(x)\,, \tag{6.1}$$

where $\varphi = \phi_1$ is the endpoint of the path in the set of diffeomorphisms, $\mathrm{Diff}(D)$, with the initial condition $\phi_0 = \mathrm{id}$. Once v_t has been found, we can solve for ϕ_1 by integrating (6.1). We can see from (6.1) that a distance metric on $\mathrm{Diff}(D)$ can be defined by

$$d(\varphi_0, \varphi_1) = \inf\left\{ \int_0^1 \|v_t\|_V \, dt \;:\; \varphi_1 = \phi_1^v \circ \varphi_0 \right\}. \tag{6.2}$$

This metric induces a metric between images which have been registered by ϕ_1^v.

Using the concepts just described, the LDDMM cost function is defined by

$$\mathcal{E}(v_t) := \underbrace{\sigma \int_0^1 \|v_t\|_V^2 dt}_{\mathcal{E}_1(v_t)} + \underbrace{\|F \circ \phi^v_{1\,*}\alpha_0 - b\|^2_{L^2(M)}}_{\mathcal{E}_2(v_t)}\,. \tag{6.3}$$

---

[1] A smooth bijective mapping with smooth inverse.

We can see that $\mathcal{E}_1$ penalizes diffeomorphisms which deviate significantly from id and $\mathcal{E}_2$ is a data fidelity term. The inner product between velocity fields in V is related to the L^2 inner product through $\langle v, w\rangle_V := \langle Lv, Lw\rangle_{L^2(D)}$, where $L := -\eta\Delta + \mathrm{id}$ which operates separately on each component of the vector field. The reproducing kernel Hilbert-space (RKHS) property, $\langle v, w\rangle_{L^2} = \langle \mathcal{K}v, w\rangle_V$, will be used to obtain the Hilbert-space gradient.

Initially, the amplitude of α_0 is unknown. Instead of trying to determine this amplitude, we use a cost function which is invariant with respect to this property. A cost function with this property is the cross-correlation

$$\mathcal{E}_2(v_t) := \frac{-\left\langle \bar{\beta}^v, \bar{b}\right\rangle^2_{L^2(M)}}{2\,\|\bar{\beta}^v\|^2_{L^2(M)}\,\|\bar{b}\|^2_{L^2(M)}} = \frac{-A^2}{2BC}\,, \tag{6.4}$$

where $\beta^v := F \circ \phi^v_{1\,*}\alpha_0$ and $\bar{b} := b - \mu_b$ measures the deviation from its average value, μ_b, and likewise for $\bar{\beta}^v$. In addition, local averages can also be used for $\bar{b}$ and $\bar{\beta}^v$ [130], but this will not be explored here.

The method uses the gradient descent approach to update the velocity fields through the equation: $v^{k+1}_t = v^k_t - a^k \nabla\mathcal{E}(v^k_t)$, where $a^k \in \mathbb{R}$ is the step size and k is the iteration number. The gradient is determined through the calculation of the Gâteaux derivative

$$\partial\mathcal{E}(v; h) := \left.\frac{d}{d\epsilon}\right|_{\epsilon=0} \mathcal{E}(v + \epsilon h)\,, \tag{6.5}$$

which is related to the Fréchet derivative (gradient) through:

$$\partial\mathcal{E}(v; h) = \int_0^1 \langle \nabla\mathcal{E}, h\rangle_V \; dt\,. \tag{6.6}$$

Note that the inner product in V is used instead of the usual L^2 inner product; this introduces $\mathcal{K}$ through the RKHS property which smooths the velocity updates and ensures that φ is a diffeomorphism.

Computing $\nabla\mathcal{E}$ for the cost function defined in (6.3) we find

$$\nabla\mathcal{E}(v_t) = 2\sigma v_t + \begin{cases} -2\mathcal{K}\{R' \circ \phi^v_{t,1} \times \nabla(I_0 \circ \phi^v_{t,0})|D\phi^v_{t,1}|\}\,, & \alpha_i \in \Omega^0(D) \\ \;\;\, 2\mathcal{K}\{I_0 \circ \phi^v_{t,0} \times \nabla(R' \circ \phi^v_{t,1})\,|D\phi^v_{t,0}|\}\,, & \alpha_i \in \Omega^n(D) \end{cases}\,, \tag{6.7}$$

where $\phi^v_{r,s} := \phi^v_s \circ (\phi^v_r)^{-1}$ and $R'(v) := \langle R, \nabla F(\phi^v_{1\,*}\alpha_0)\rangle_{L^2(M)}$ is the inverse Fourier transform of the residual, R, which has retained the phase from $\mathcal{F}\phi^v_{1\,*}\alpha_0$. We can see this by inspecting the gradient of the forward operator, $\nabla F\,(\alpha) = \mathrm{Re}\,\frac{\tilde{\alpha}}{|\tilde{\alpha}|}\,\Phi^*$, where Φ^* is the complex conjugate of the kernel related to the Fourier transform. The gradient for the cross-correlation function, defined in (6.4), is obtained through the substitution: $R' \to \frac{A}{BC}\left(\frac{A}{B}\,\bar{\beta}'^{\,v} - \bar{b}'\right)$. As we expect, when $F = \mathrm{id}$, this method recovers the direct LDDMM registration procedure. This will be used in the next section to highlight some of the differences between the direct and indirect procedures.

6.2 Numerical performance

In this section, the numerical performance of the algorithm based on the geometric and mass-preserving actions will be illustrated. The first example shows a comparison between the direct geometric method – where the target image is known – and the indirect methods. The results illustrate the effect of translational invariance on the indirect methods as well as the difference between the two actions. The final example compares the method to $\text{ER}_{50}\text{HIO}_{100}$ with shrinkwrap for low-SNR measurements showing a potential area of application.

Results from the first example are shown in Fig. 6.1. In this example, the template image “J” is registered to the target “V” using the diffraction pattern shown in Fig. 6.1(c). The algorithm in each instance was run for 1000 iterations with $\sigma = 10^{-3}$, $\eta = 5\times10^{-3}$, 10 time steps and variable step size to maintain $\|a^k \, \nabla\mathcal{E}(v_t^k)\|_\infty = 500^{-1}$. Figure 6.1(d–f) and Fig. 6.1(g–i) show the time evolution for the indirect registration methods using the geometric and mass-preserving actions respectively. A comparison between the direct geometric, indirect geometric and mass-preserving displacements are shown in Fig. 6.1(j–l) with the corresponding warps shown in Fig. 6.1(m–o). We can see the effect of translational invariance on the registration result by comparing the direct and indirect results shown in Fig. 6.1(j,m) and Fig. 6.1(k,n) respectively. The translational invariance removes the need to align the images prior to registration. Additionally, we can see that the mass-preserving method, due to mass conservation, must transport the density from the top right of the “J” all the way to the top left of the “V” which can be seen in Fig. 6.1(l).

The final simulation is shown in Fig. 6.2 which provides a potential application to singleshot imaging where an initial higher-SNR image is acquired of the static sample and used to obtain sample dynamics from low-SNR measurements. The template and target images are the same as the previous example and all the parameters are the same except for $\eta = 2 \times 10^{-2}$ which was used to improve the noise robustness. Diffraction measurements with only Poisson and Poisson with additive Gaussian noise are shown in Fig. 6.2(a,b) and Fig. 6.2(c,d), respectively with the SNR (dB) denoted in the lower left corners. Reconstructions from $\text{ER}_{50}\text{HIO}_{100}$ with shrinkwrap is shown in Fig. 6.2(e–l) with fixed and varying shrinkwrap thresholds. Twenty independent reconstructions were found and compared to the true image to determine the best reconstructions. This is clearly an ideal situation which would not be possible experimentally. The last row shows the reconstructions obtained with the indirect registration method using the geometric action. We can see, even compared to the best of 20 reconstructions of $\text{ER}_{50}\text{HIO}_{100}$, that the registration method performs favorably.

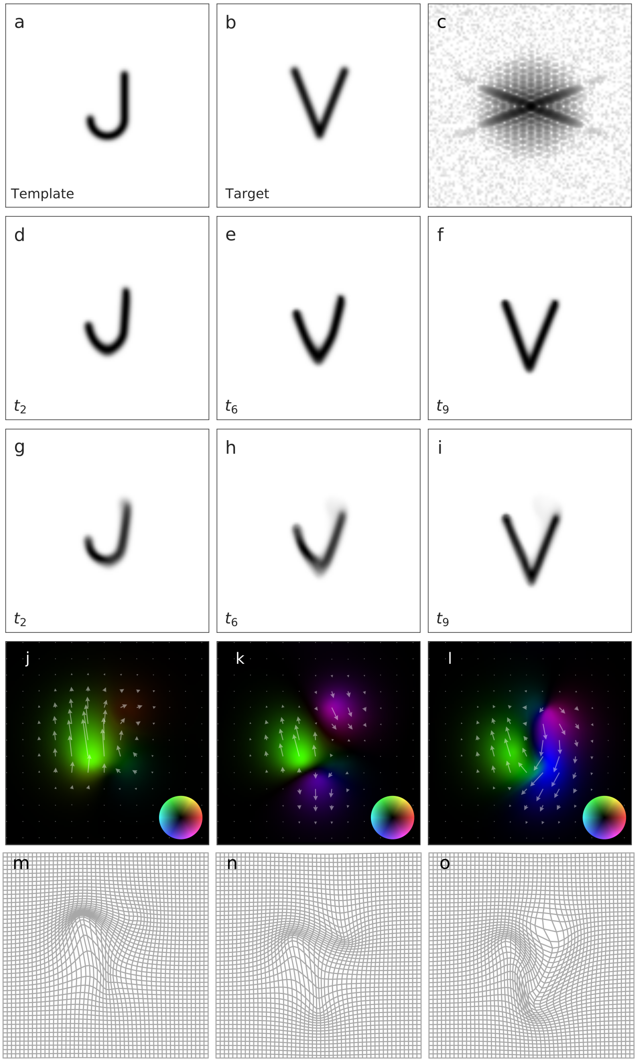

Figure 6.1: Comparison between different registration techniques. (a) Initial template image used to match (b) the target image indirectly through (c) the target's diffraction pattern. The temporal evolution for the geometric (d–f) and mass-preserving (g–i) actions. (j–l) Displacement vectors and (m–o) deformations associated with direct geometric, indirect geometric and mass-preserving methods respectively. Figure adapted from Paper III.

6.3 Extensions

While we can see that this method is capable of phase retrieval, it is important to note some of the current drawbacks which restrict its application. Possibly the largest drawback of this method is that it has been formulated for real images. In the majority of situations, the ESW acquires phase from the transmission of the field through a sample of finite thickness. Two approaches could be used to remedy the

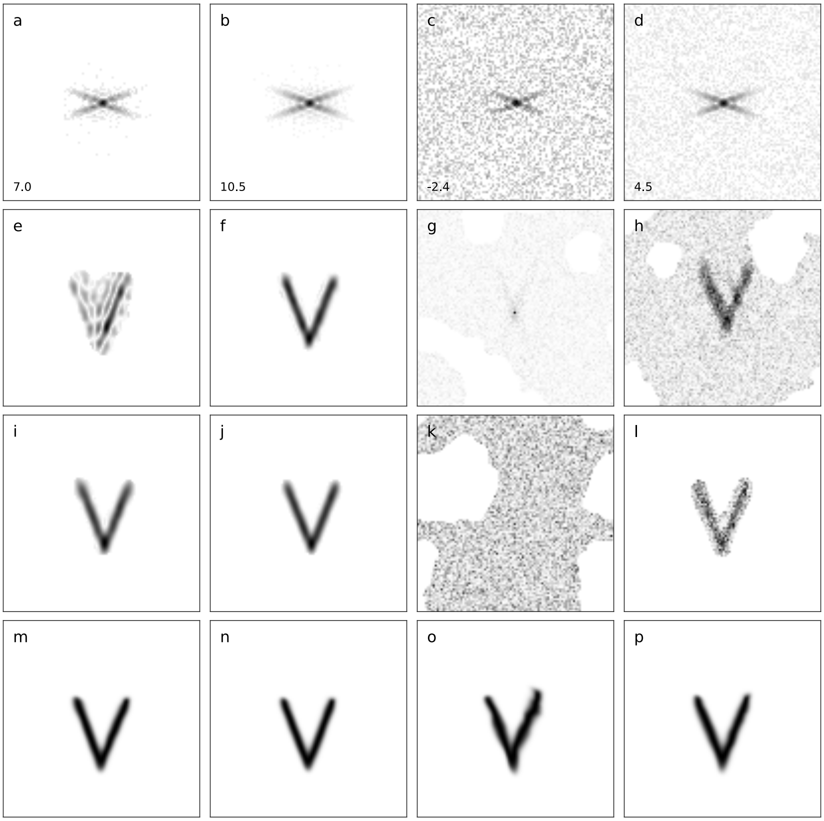

Figure 6.2: Comparison between $\mathrm{ER}_{50}\mathrm{HIO}_{100}$ with shrinkwrap and geometric-action registration method for low-SNR measurements. (a–d) Diffraction measurements with (a,b) Poisson noise and with (c,d) both Poisson and Gaussian noise. The SNR (dB) is indicated in the lower-left corner. (e–h) Reconstructions from $\mathrm{ER}_{50}\mathrm{HIO}_{100}$ with a shrinkwrap threshold of 0.15. (i–l) Reconstructions from $\mathrm{ER}_{50}\mathrm{HIO}_{100}$ with varying shrinkwrap thresholds of $\{0.2, 0.2, 0.4, 0.35\}$ respectively. (m–p) Reconstructions obtained using the indirect LDDMM registration method. Figure adapted from Paper III.

situation: first, we could treat the electron density or material thickness and modify the forward operator to account for sample transmission. This method would have a natural extension into recovering the electron density in 3D. Alternatively, we could extend the method to included complex-valued images and treat the ESW directly. When studying a dynamic sample, it is possible to start with a complex-valued template and use the same procedure. It could also be possible to register the magnitude and phase of the ESW separately. Splitting the ESW into real and imaginary parts seems unfavorable as the relative proportion of each would have to be known a priori.

Another major drawback is that the method uses a gradient descent approach to update v_t which means the method finds local minima with no guarantee that it corresponds to the global minimum. It has been observed that the procedure based on the geometric action is more likely to find the global minimum due to its smaller subset of possible solutions (orbit); a notable exception to this is shown in an example in Paper III which illustrates the importance of using the autocorrelation function for constructing the template. Other potential extensions include multi-scale methods [131, 132] or a metamorphosis action [133, 125]. There is a large literature describing different methods for non-rigid registration which could serve as a guide for potential improvements.

7

Summary and outlook

The thesis presents work on the application, understanding, and extension of the FTH and CDI methods. These two methods are important in the field of short-wavelength microscopy due to their ability to image dynamic samples with nanometer spatial resolution. The methods take different approaches to reconstructing the sample, but often have very similar experimental setups which allows for hybrid approaches[1] to utilize the advantages of both techniques.

The reconstruction quality within a mask-based FTH experiment depends critically on the shape of the reference apertures. In Paper IV, we studied the effects related to the reference aperture's 3D structure on the reconstruction. We gained insight into these effects by performing phase retrieval on diffraction data from apertures with varying shapes and through comparisons with multislice simulations. By simulating FTH experiments, we were able to determine various aspects such as the resolution and reconstruction plane. This also provided insights into how the reference aperture should be fabricated and the post-processing steps which should be performed to optimize the reconstruction quality.

In Papers I and II, the extension of CDI to multi-wavelength diffraction data was studied. A model was presented to describe the multi-wavelength effects and double-slit diffraction data were used to extract the spectral and coherence properties of a HHG source. This was then used to validate the model by comparing calculated and experimental diffraction patterns. The coherence properties were used to extract quasi-monochromatic data which was reconstructed using different methods. The method was generalized in Paper II by allowing the exit waves from each wavelength to be recovered separately. Experimentally, the exit waves may vary due to beamline optics which affect the incoming wavefronts or due to the wavelength dependence of

---

[1] Which refines the FTH reconstruction using iterative phase retrieval.

the sample transmission. A number of sources, which include HHG and undulator-based sources, have multiple harmonics which could make this technique widely applicable.

In Paper III, the phase retrieval problem was approached from an image registration perspective. Starting with an initial guess, the problem is to find a transformation which warps the guess until its diffraction pattern matches the data. The method does not rely on a sample support estimate which is often the main issue associated with iterative phase retrieval algorithms. Numerical simulations were presented to illustrate the algorithm performance under different circumstances.

As computational resources become cheaper and more available, it seems inevitable that we will be able to tackle more complicated and higher dimensional problems in the future. As a step in this direction, the next section looks at the possibility of extending phase retrieval to 3D surfaces and some of the complications which arise.

7.1 Phase retrieval on arbitrary closed surfaces

Next, we consider the problem of recovering a field on an arbitrary closed surface and compare it to the conventional 2D phase retrieval problem. This example illustrates some aspects of inverse problems which did not need to considered for the 2D phase retrieval problem.

Returning to Section 2.2, we recall that the far fields for 2D and 3D samples are given by

$$\hat{u} = \mathcal{F}u \tag{7.1}$$

$$\hat{u} = -\mathcal{S}_k \partial_n^+ u + \mathcal{D}_k \gamma^+ u \,, \tag{7.2}$$

respectively. In 2D, the Fourier transform operates on u which is constrained to the sample plane, while its 3D counterpart operates on the Cauchy data, $c_+ u$, specified over the sample's 3D surface, $\partial\Omega$. A sketch of the geometry of the 3D problem is shown in Fig. 7.1.

In addition to the existence and uniqueness questions which exist for the 2D phase retrieval problem, the 3D problem has an additional issue related to numerical instability. This can be seen by comparing the singular values of the forward operators. The singular values[2], μ_n, can be used to characterize the numerical stability as the inverse is proportional to μ_n^{-1} [134, 37]. The Bempp package [135, 136, 137] was used to construct the 3D discrete forward operator for two different sample-detector distances. The singular values are plotted in Fig. 7.2 for the two geometries along with those of the 2D Fourier transform[3]. The large condition number[4] means reg-

---

[2] Which are solutions to $A^\dagger A \varphi_n = \mu_n^2 \varphi_n$, where A is the forward operator described by either (7.1) or (7.2).

[3] The Fourier transform being unitary results in $\mu_n = 1$.

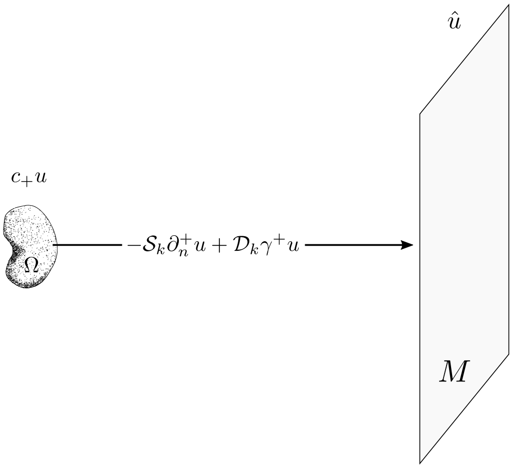

Figure 7.1: 3D phase retrieval geometry (not to scale) where the Cauchy data, $c_+ u$, on the surface of the sample, $\partial\Omega$, is mapped to the far field, $\hat{u}$ on the detector, M.

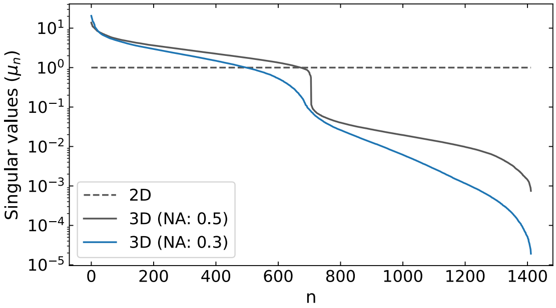

Figure 7.2: Singular values for the 2D and 3D far field operators described by (7.1) and (7.2).

ularization techniques must be used to ensure numerical stability. On the other hand, by venturing into 3D, we have gained an additional constraint which we did not have in the 2D problem; that is, the field must fulfill the Helmholtz equation. This constraint can be included directly into the algorithm through the Calderón projection [38], Π_C. Now, a potential alternating projection scheme for recovering the phase is given by $u^{n+1} = \Pi_C \, \Pi_S \, \Pi_M u^n$ which could be paired with shape optimization approaches for updating the obstacle shape [138, 139, 37, 129].

By extending the method into 3D we have increased the ill-posedness of the problem which could be offset by acquiring additional diversity measurements or by exploiting sparsity and additional knowledge about the problem. Interestingly, we gain an additional constraint which can be incorporated directly into the phase retrieval algorithm to possibly improve the quality of the solution. Lastly, solving 3D inverse problem relies heavily on the availability of fast numerical solvers of the forward problem.

---

[4] The ratio between the first and last singular values, $\text{Cond} = \mu_1/\mu_N \sim 10^6$.

A

Differential forms

In this appendix some notation and concepts related to differential forms are introduced which are necessary for Chapter 6. The notation used here and in Chapter 6 follow that of [127]. Differential forms play an important role in physics and mathematics as they are the quantities being integrated in vector calculus which are more familiarly written as $\dots dx$, $\dots dS$ or $\dots dV$.

Differential p-forms, $\Omega^p(D)$, over an n-dimensional manifold, D, are antisymmetric tensors, which, in component form are specified by

$$\alpha = \frac{1}{p!}\,\alpha_{i\dots j}(x)\,dx^i \wedge \cdots \wedge dx^j\,. \tag{A.1}$$

In particular, we will focus on zero-forms (functions), $\Omega^0\left(D\right)$, and volume-forms, $\Omega^n\left(D\right)$, which are given by

$$\alpha\left(x\right) = \begin{cases} a(x) & \alpha \in \Omega^0(D) \\ a\left(x\right)\mathrm{vol}_g & \alpha \in \Omega^n(D) \end{cases} \tag{A.2}$$

for a function, $a : D \to \mathbb{R}$ and $x \in D$. The components of the metric volume form are ${\mathrm{vol}_g}_{i\dots j} = \sqrt{|g|}\,\epsilon_{i\dots j}$ in a right-handed coordinate system with metric tensor, g, and the usual Levi-Civita symbol, $\epsilon_{i\dots j}$. This can be written in another form using a basis of 1-forms, e^i, as $\mathrm{vol}_g = e^1 \wedge \cdots \wedge e^n$.

The exterior (wedge) product is a mapping which takes two differential forms and returns another form. Taking a p and q-form as arguments, it can be regarded as a mapping $\wedge : \Omega^p(D) \times \Omega^q(D) \to \Omega^{p+q}(D)$ defined by

$$\wedge := \frac{(p+q)!}{p!q!}\pi^A \circ \otimes\,, \tag{A.3}$$

which is analogous to the direct product, $\otimes$, for tensors, but ensures that the result is a differential form in $\Omega^{p+q}(D)$. The π^A operator ensures that $\wedge$ returns an antisymmetric tensor which in component form is $(\pi_A t)_{a\ldots b} = t_{[a\ldots b]}$, where the square brackets denote antisymmetrization of the indices (e.g. $t_{[ab]} = \frac{1}{2!}(t_{ab} - t_{ba})$).

Associated with each diffeomorphism are operations for transforming the differential forms on D in either the forward (push-forward) or backward (pull-back) directions. For a diffeomorphism, $\varphi \in \mathrm{Diff}(D) : D \to D$, the pull-back operation is

$$\varphi^* \alpha = \begin{cases} a \circ \varphi & \alpha \in \Omega^0(D) \\ \sqrt{|D\varphi|}\, a \circ \varphi \,\mathrm{vol}_g & \alpha \in \Omega^n(D) \end{cases} . \tag{A.4}$$

Above, $a : D \to \mathbb{R}$ is a function and $|D\varphi|$ is the Jacobian determinant. The pull-back and push-forward operations are related through $\varphi^*\alpha = (\varphi^{-1})_*\,\alpha$. The different expressions for the pull-back operations for zero and volume forms lead to the geometric and mass-preserving registration procedures described in Chapter 6 and Paper III.

Bibliography

[1] Sadao Aoki and Seishi Kikuta. X-ray holographic microscopy. *Japanese Journal of Applied Physics*, 13(9):1385–1392, September 1974.

[2] Jianwei Miao, Pambos Charalambous, Janos Kirz, and David Sayre. Extending the methodology of x-ray crystallography to allow imaging of micrometre-sized non-crystalline specimens. *Nature*, 400(6742):342–344, July 1999.

[3] Richard L. Sandberg, Ariel Paul, Daisy A. Raymondson, Steffen Hädrich, David M. Gaudiosi, Jim Holtsnider, Ra'anan I. Tobey, Oren Cohen, Margaret M. Murnane, Henry C. Kapteyn, Changyong Song, Jianwei Miao, Yanwei Liu, and Farhad Salmassi. Lensless diffractive imaging using tabletop coherent high-harmonic soft-x-ray beams. *Phys. Rev. Lett.*, 99:098103, August 2007.

[4] Ofer Kfir, Sergey Zayko, Christina Nolte, Murat Sivis, Marcel Möller, Birgit Hebler, Sri Sai Phani Kanth Arekapudi, Daniel Steil, Sascha Schäfer, Manfred Albrecht, Oren Cohen, Stefan Mathias, and Claus Ropers. Nanoscale magnetic imaging using circularly polarized high-harmonic radiation. *Science Advances*, 3(12), 2017.

[5] G. J. Williams, H. M. Quiney, B. B. Dhal, C. Q. Tran, K. A. Nugent, A. G. Peele, D. Paterson, and M. D. de Jonge. Fresnel coherent diffractive imaging. *Phys. Rev. Lett.*, 97:025506, July 2006.

[6] I. K. Robinson, I. A. Vartanyants, G. J. Williams, M. A. Pfeifer, and J. A. Pitney. Reconstruction of the shapes of gold nanocrystals using coherent x-ray diffraction. *Phys. Rev. Lett.*, 87:195505, October 2001.

[7] G. J. Williams, M. A. Pfeifer, I. A. Vartanyants, and I. K. Robinson. Three-dimensional imaging of microstructure in au nanocrystals. *Phys. Rev. Lett.*, 90:175501, April 2003.

[8] Mark A. Pfeifer, Garth J. Williams, Ivan A. Vartanyants, Ross Harder, and Ian K. Robinson. Three-dimensional mapping of a deformation field inside a nanocrystal. *Nature*, 442(7098):63–66, July 2006.

[9] Ian Robinson and Ross Harder. Coherent x-ray diffraction imaging of strain at the nanoscale. *Nature Materials*, 8(4):291–298, April 2009.

[10] Dmitry Karpov and Edwin Fohtung. Bragg coherent diffractive imaging of strain at the nanoscale. *Journal of Applied Physics*, 125(12):121101, 2019.

[11] J. M. Rodenburg, A. C. Hurst, A. G. Cullis, B. R. Dobson, F. Pfeiffer, O. Bunk, C. David, K. Jefimovs, and I. Johnson. Hard-x-ray lensless imaging of extended objects. *Phys. Rev. Lett.*, 98:034801, January 2007.

[12] Pierre Thibault, Martin Dierolf, Andreas Menzel, Oliver Bunk, Christian David, and Franz Pfeiffer. High-resolution scanning x-ray diffraction microscopy. *Science*, 321(5887):379–382, 2008.

[13] R. W. Gerchberg and W. O. Saxton. A practical algorithm for the determination of phase from image and diffraction plane pictures. *Optik*, 1972.

[14] J. R. Fienup. Reconstruction of an object from the modulus of its fourier transform. *Opt. Lett.*, 3(1):27–29, July 1978.

[15] B Reuter and H Mahr. Experiments with fourier transform holograms using 4.48 nm x-rays. *Journal of Physics E: Scientific Instruments*, 9(9):746–751, sep 1976.

[16] Ian McNulty, Janos Kirz, Chris Jacobsen, Erik H. Anderson, Malcolm R. Howells, and Dieter P. Kern. High-resolution imaging by fourier transform x-ray holography. *Science*, 256(5059):1009–1012, 1992.

[17] S. Eisebitt, J. Lüning, W. F. Schlotter, M. Lörgen, O. Hellwig, W. Eberhardt, and J. Stöhr. Lensless imaging of magnetic nanostructures by x-ray spectro-holography. *Nature*, 432:885, December 2004.

[18] David Shapiro, Pierre Thibault, Tobias Beetz, Veit Elser, Malcolm Howells, Chris Jacobsen, Janos Kirz, Enju Lima, Huijie Miao, Aaron M. Neiman, and David Sayre. Biological imaging by soft x-ray diffraction microscopy. *Proceedings of the National Academy of Sciences*, 102(43):15343–15346, 2005.

[19] Pierre Thibault, Veit Elser, Chris Jacobsen, David Shapiro, and David Sayre. Reconstruction of a yeast cell from X-ray diffraction data. *Acta Crystallographica Section A*, 62(4):248–261, July 2006.

[20] M. Marvin Seibert, Tomas Ekeberg, Filipe R. N. C. Maia, Martin Svenda, Jakob Andreasson, Olof Jönsson, Duško Odić, Bianca Iwan, Andrea Rocker, Daniel Westphal, Max Hantke, Daniel P. DePonte, Anton Barty, Joachim Schulz, Lars Gumprecht, Nicola Coppola, Andrew Aquila, Mengning Liang, Thomas A. White, Andrew Martin, Carl Caleman, Stephan Stern, Chantal Abergel, Virginie Seltzer, Jean-Michel Claverie, Christoph Bostedt, John D. Bozek, Sébastien Boutet, A. Alan Miahnahri, Marc Messerschmidt, Jacek Krzywinski, Garth Williams, Keith O. Hodgson, Michael J. Bogan,

Christina Y. Hampton, Raymond G. Sierra, Dmitri Starodub, Inger Andersson, Saša Bajt, Miriam Barthelmess, John C. H. Spence, Petra Fromme, Uwe Weierstall, Richard Kirian, Mark Hunter, R. Bruce Doak, Stefano Marchesini, Stefan P. Hau-Riege, Matthias Frank, Robert L. Shoeman, Lukas Lomb, Sascha W. Epp, Robert Hartmann, Daniel Rolles, Artem Rudenko, Carlo Schmidt, Lutz Foucar, Nils Kimmel, Peter Holl, Benedikt Rudek, Benjamin Erk, André Hömke, Christian Reich, Daniel Pietschner, Georg Weidenspointner, Lothar Strüder, Günter Hauser, Hubert Gorke, Joachim Ullrich, Ilme Schlichting, Sven Herrmann, Gerhard Schaller, Florian Schopper, Heike Soltau, Kai-Uwe Kühnel, Robert Andritschke, Claus-Dieter Schröter, Faton Krasniqi, Mario Bott, Sebastian Schorb, Daniela Rupp, Marcus Adolph, Tais Gorkhover, Helmut Hirsemann, Guillaume Potdevin, Heinz Graafsma, Björn Nilsson, Henry N. Chapman, and Janos Hajdu. Single mimivirus particles intercepted and imaged with an x-ray laser. *Nature*, 470(7332):78–81, February 2011.

[21] Tomas Ekeberg, Martin Svenda, Chantal Abergel, Filipe R. N. C. Maia, Virginie Seltzer, Jean-Michel Claverie, Max Hantke, Olof Jönsson, Carl Nettelblad, Gijs van der Schot, Mengning Liang, Daniel P. DePonte, Anton Barty, M. Marvin Seibert, Bianca Iwan, Inger Andersson, N. Duane Loh, Andrew V. Martin, Henry Chapman, Christoph Bostedt, John D. Bozek, Ken R. Ferguson, Jacek Krzywinski, Sascha W. Epp, Daniel Rolles, Artem Rudenko, Robert Hartmann, Nils Kimmel, and Janos Hajdu. Three-dimensional reconstruction of the giant mimivirus particle with an x-ray free-electron laser. *Phys. Rev. Lett.*, 114:098102, Mar 2015.

[22] Tais Gorkhover, Anatoli Ulmer, Ken Ferguson, Max Bucher, Filipe R. N. C. Maia, Johan Bielecki, Tomas Ekeberg, Max F. Hantke, Benedikt J. Daurer, Carl Nettelblad, Jakob Andreasson, Anton Barty, Petr Bruza, Sebastian Carron, Dirk Hasse, Jacek Krzywinski, Daniel S. D. Larsson, Andrew Morgan, Kerstin Mühlig, Maria Müller, Kenta Okamoto, Alberto Pietrini, Daniela Rupp, Mario Sauppe, Gijs van der Schot, Marvin Seibert, Jonas A. Sellberg, Martin Svenda, Michelle Swiggers, Nicusor Timneanu, Daniel Westphal, Garth Williams, Alessandro Zani, Henry N. Chapman, Gyula Faigel, Thomas Möller, Janos Hajdu, and Christoph Bostedt. Femtosecond x-ray fourier holography imaging of free-flying nanoparticles. *Nature Photonics*, 12(3):150–153, March 2018.

[23] Ashish Tripathi, Jyoti Mohanty, Sebastian H. Dietze, Oleg G. Shpyrko, Erik Shipton, Eric E. Fullerton, Sang Soo Kim, and Ian McNulty. Dichroic coherent diffractive imaging. *Proceedings of the National Academy of Sciences*, 108(33):13393–13398, 2011.

[24] Felix Büttner, C. Moutafis, M. Schneider, B. Krüger, C. M. Günther, J. Geilhufe, C. v. Korff Schmising, J. Mohanty, B. Pfau, S. Schaffert, A. Bisig, M. Foerster, T. Schulz, C. A. F. Vaz, J. H. Franken, H. J. M. Swagten, M. Kläui, and S. Eisebitt. Dynamics and inertia of skyrmionic spin structures. *Nature Physics*, 11(3):225–228, March 2015.

[25] D. Russell. Luke, James V. Burke, and Richard G. Lyon. Optical wavefront reconstruction: Theory and numerical methods. *SIAM Review*, 44(2):169–224, 2002.

[26] S. Marchesini. Invited article: A unified evaluation of iterative projection algorithms for phase retrieval. *Review of Scientific Instruments*, 78(1):011301, 2007.

[27] Henry N. Chapman and Keith A. Nugent. Coherent lensless x-ray imaging. *Nature Photonics*, 4(12):833–839, December 2010.

[28] H.M. Quiney. Coherent diffractive imaging using short wavelength light sources. *Journal of Modern Optics*, 57(13):1109–1149, 2010.

[29] Stefano Marchesini and David Shapiro. *Coherent X-Ray Diffraction Microscopy*, chapter 5, pages 119–168. John Wiley & Sons, Ltd, 2010.

[30] Bastian Pfau and Stefan Eisebitt. *X-Ray Holography*, pages 1–36. Springer International Publishing, Cham, 2014.

[31] Jianwei Miao, Tetsuya Ishikawa, Ian K. Robinson, and Margaret M. Murnane. Beyond crystallography: Diffractive imaging using coherent x-ray light sources. *Science*, 348(6234):530–535, 2015.

[32] Y. Shechtman, Y. C. Eldar, O. Cohen, H. N. Chapman, J. Miao, and M. Segev. Phase retrieval with application to optical imaging: A contemporary overview. *IEEE Signal Processing Magazine*, 32(3):87–109, 2015.

[33] Zhibin Sun, Jiadong Fan, Haoyuan Li, and Huaidong Jiang. Current status of single particle imaging with x-ray lasers. *Applied Sciences*, 1(1), 01 2018.

[34] John David Jackson. *Classical electrodynamics.* Third edition. New York : Wiley, 1999.

[35] J.W. Goodman. *Introduction to Fourier Optics.* McGraw-Hill physical and quantum electronics series. W. H. Freeman, 2005.

[36] David Paganin. *Coherent X-Ray Optics (Oxford Series on Synchrotron Radiation).* Oxford University Press, 2006.

[37] Rainer Kress David Colton. *Inverse Acoustic and Electromagnetic Scattering Theory.* Springer-Verlag New York, 3 edition, 2013.

[38] Simon N. Chandler-Wilde, Ivan G. Graham, Stephen Langdon, and Euan A. Spence. Numerical-asymptotic boundary integral methods in high-frequency acoustic scattering. *Acta Numerica*, 21:89–305, 2012.

[39] Avinash C. Kak and Malcolm. Slaney. *Principles of Computerized Tomographic Imaging.* Society for Industrial and Applied Mathematics, 2001.

[40] Pierre Thibault. Feasibility of 3d reconstructions from a single 2d diffraction measurement. *arXiv e-prints*, page arXiv:0909.1643, Sep 2009.

[41] Kevin S. Raines, Sara Salha, Richard L. Sandberg, Huaidong Jiang, Jose A. Rodríguez, Benjamin P. Fahimian, Henry C. Kapteyn, Jincheng Du, and Jianwei Miao. Three-dimensional structure determination from a single view. *Nature*, 463(7278):214–217, January 2010.

[42] P. Villanueva-Perez, B. Pedrini, R. Mokso, P. Vagovic, V. A. Guzenko, S. J. Leake, P. R. Willmott, P. Oberta, C. David, H. N. Chapman, and M. Stampanoni. Hard x-ray multi-projection imaging for single-shot approaches. *Optica*, 5(12):1521–1524, Dec 2018.

[43] J. Duarte, R. Cassin, J. Huijts, B. Iwan, F. Fortuna, L. Delbecq, H. Chapman, M. Fajardo, M. Kovacev, W. Boutu, and H. Merdji. Computed stereo lensless x-ray imaging. *Nature Photonics*, 13(7):449–453, July 2019.

[44] Henry N. Chapman, Anton Barty, Stefano Marchesini, Aleksandr Noy, Stefan P. Hau-Riege, Congwu Cui, Malcolm R. Howells, Rachel Rosen, Haifeng He, John C. H. Spence, Uwe Weierstall, Tobias Beetz, Chris Jacobsen, and David Shapiro. High-resolution ab initio three-dimensional x-ray diffraction microscopy. *J. Opt. Soc. Am. A*, 23(5):1179–1200, May 2006.

[45] S. Eisebitt, M. Lörgen, W. Eberhardt, J. Lüning, J. Stöhr, C. T. Rettner, O. Hellwig, E. E. Fullerton, and G. Denbeaux. Polarization effects in coherent scattering from magnetic specimen: Implications for x-ray holography, lensless imaging, and correlation spectroscopy. *Phys. Rev. B*, 68:104419, September 2003.

[46] Joachim Stohr and Hans Christoph Siegmann. *Magnetism: From Fundamentals to Nanoscale Dynamics.* Springer-Verlag Berlin Heidelberg, 1 edition, 2006.

[47] J. P. Hannon, G. T. Trammell, M. Blume, and Doon Gibbs. X-ray resonance exchange scattering. *Phys. Rev. Lett.*, 61:1245–1248, Sep 1988.

[48] J. M. Cowley and A. F. Moodie. The scattering of electrons by atoms and crystals. I. A new theoretical approach. *Acta Crystallographica*, 10(10):609–619, October 1957.

[49] Kenan Li, Michael Wojcik, and Chris Jacobsen. Multislice does it all-calculating the performance of nanofocusing x-ray optics. *Opt. Express*, 25(3):1831–1846, February 2017.

[50] Peter R. T. Munro. Rigorous multi-slice wave optical simulation of x-ray propagation in inhomogeneous space. *J. Opt. Soc. Am. A*, 36(7):1197–1208, July 2019.

[51] Akihiro Suzuki, Shin Furutaku, Kei Shimomura, Kazuto Yamauchi, Yoshiki Kohmura, Tetsuya Ishikawa, and Yukio Takahashi. High-resolution multislice x-ray ptychography of extended thick objects. *Phys. Rev. Lett.*, 112:053903, February 2014.

[52] M. Lewenstein, Ph. Balcou, M. Yu. Ivanov, Anne L'Huillier, and P. B. Corkum. Theory of high-harmonic generation by low-frequency laser fields. *Phys. Rev. A*, 49:2117–2132, March 1994.

[53] David Attwood. *Soft X-Rays and Extreme Ultraviolet Radiation: Principles and Applications.* Cambridge University Press, 1999.

[54] Takashi Tanaka and Hideo Kitamura. *SPECTRA*: a synchrotron radiation calculation code. *Journal of Synchrotron Radiation*, 8(6):1221–1228, November 2001.

[55] Ferenc Krausz and Misha Ivanov. Attosecond physics. *Rev. Mod. Phys.*, 81:163–234, February 2009.

[56] C M Heyl, C L Arnold, A Couairon, and A L'Huillier. Introduction to macroscopic power scaling principles for high-order harmonic generation. *Journal of Physics B: Atomic, Molecular and Optical Physics*, 50(1):013001, December 2016.

[57] B. Manschwetus, L. Rading, F. Campi, S. Maclot, H. Coudert-Alteirac, J. Lahl, H. Wikmark, P. Rudawski, C. M. Heyl, B. Farkas, T. Mohamed, A. L'Huillier, and P. Johnsson. Two-photon double ionization of neon using an intense attosecond pulse train. *Phys. Rev. A*, 93:061402, Jun 2016.

[58] P. B. Corkum. Plasma perspective on strong field multiphoton ionization. *Phys. Rev. Lett.*, 71:1994–1997, September 1993.

[59] K. J. Schafer, Baorui Yang, L. F. DiMauro, and K. C. Kulander. Above threshold ionization beyond the high harmonic cutoff. *Phys. Rev. Lett.*, 70:1599–1602, March 1993.

[60] Boris Vodungbo, Anna Barszczak Sardinha, Julien Gautier, Guillaume Lambert, Constance Valentin, Magali Lozano, Grégory Iaquaniello, Franck Delmotte, Stéphane Sebban, Jan Lüning, and Philippe Zeitoun. Polarization control of high order harmonics in the euv photon energy range. *Opt. Express*, 19(5):4346–4356, Feb 2011.

[61] Avner Fleischer, Ofer Kfir, Tzvi Diskin, Pavel Sidorenko, and Oren Cohen. Spin angular momentum and tunable polarization in high-harmonic generation. *Nature Photonics*, 8(7):543–549, July 2014.

[62] Ofer Kfir, Patrik Grychtol, Emrah Turgut, Ronny Knut, Dmitriy Zusin, Dimitar Popmintchev, Tenio Popmintchev, Hans Nembach, Justin M. Shaw, Avner Fleischer, Henry Kapteyn, Margaret Murnane, and Oren Cohen. Generation of bright phase-matched circularly-polarized extreme ultraviolet high harmonics. *Nature Photonics*, 9(2):99–105, February 2015.

[63] Daniel D. Hickstein, Franklin J. Dollar, Patrik Grychtol, Jennifer L. Ellis, Ronny Knut, Carlos Hernández-García, Dmitriy Zusin, Christian Gentry, Justin M. Shaw, Tingting Fan, Kevin M. Dorney, Andreas Becker, Agnieszka

Jaroń-Becker, Henry C. Kapteyn, Margaret M. Murnane, and Charles G. Durfee. Non-collinear generation of angularly isolated circularly polarized high harmonics. *Nature Photonics*, 9(11):743–750, November 2015.

[64] Tingting Fan, Patrik Grychtol, Ronny Knut, Carlos Hernández-García, Daniel D. Hickstein, Dmitriy Zusin, Christian Gentry, Franklin J. Dollar, Christopher A. Mancuso, Craig W. Hogle, Ofer Kfir, Dominik Legut, Karel Carva, Jennifer L. Ellis, Kevin M. Dorney, Cong Chen, Oleg G. Shpyrko, Eric E. Fullerton, Oren Cohen, Peter M. Oppeneer, Dejan B. Milošević, Andreas Becker, Agnieszka A. Jaroń-Becker, Tenio Popmintchev, Margaret M. Murnane, and Henry C. Kapteyn. Bright circularly polarized soft x-ray high harmonics for x-ray magnetic circular dichroism. *Proceedings of the National Academy of Sciences*, 112(46):14206–14211, 2015.

[65] J. J. Rocca, V. Shlyaptsev, F. G. Tomasel, O. D. Cortázar, D. Hartshorn, and J. L. A. Chilla. Demonstration of a discharge pumped table-top soft-x-ray laser. *Phys. Rev. Lett.*, 73:2192–2195, Oct 1994.

[66] Alex Rockwood, Yong Wang, Shoujun Wang, Mark Berrill, Vyacheslav N. Shlyaptsev, and Jorge J. Rocca. Compact gain-saturated x-ray lasers down to 6.85nm and amplification down to 5.85nm. *Optica*, 5(3):257–262, Mar 2018.

[67] R. L. Sandberg, D. A. Raymondson, C. La o vorakiat, A. Paul, K. S. Raines, J. Miao, M. M. Murnane, H. C. Kapteyn, and W. F. Schlotter. Tabletop soft-x-ray fourier transform holography with 50 nm resolution. *Opt. Lett.*, 34(11):1618–1620, June 2009.

[68] W. F. Schlotter, R. Rick, K. Chen, A. Scherz, J. Stöhr, J. Lüning, S. Eisebitt, Ch. Günther, W. Eberhardt, O. Hellwig, and I. McNulty. Multiple reference fourier transform holography with soft x rays. *Applied Physics Letters*, 89(16):163112, 2006.

[69] Lorenz-M. Stadler, Christian Gutt, Tina Autenrieth, Olaf Leupold, Stefan Rehbein, Yuriy Chushkin, and Gerhard Grübel. Hard x ray holographic diffraction imaging. *Phys. Rev. Lett.*, 100:245503, June 2008.

[70] S.G. Podorov, K.M. Pavlov, and D.M. Paganin. A non-iterative reconstruction method for direct and unambiguous coherent diffractive imaging. *Opt. Express*, 15(16):9954–9962, August 2007.

[71] Manuel Guizar-Sicairos and James R. Fienup. Holography with extended reference by autocorrelation linear differential operation. *Opt. Express*, 15(26):17592–17612, December 2007.

[72] Andrew V. Martin, Adrian J. D'Alfonso, Fenglin Wang, Richard Bean, Flavio Capotondi, Richard A. Kirian, Emanuele Pedersoli, Lorenzo Raimondi, Francesco Stellato, Chun Hong Yoon, and Henry N. Chapman. X-ray holography with a customizable reference. *Nature Communications*, 5(1):4661, August 2014.

[73] Stefano Marchesini, Sébastien Boutet, Anne E. Sakdinawat, Michael J. Bogan, Saša Bajt, Anton Barty, Henry N. Chapman, Matthias Frank, Stefan P. Hau-Riege, Abraham Szöke, Congwu Cui, David A. Shapiro, Malcolm R. Howells, John C. H. Spence, Joshua W. Shaevitz, Joanna Y. Lee, Janos Hajdu, and Marvin M. Seibert. Massively parallel x-ray holography. *Nature Photonics*, 2(9):560–563, September 2008.

[74] Manuel Fohler, Stefanie Frömmel, Michael Schneider, Bastian Pfau, Christian M. Günther, Martin Hennecke, Erik Guehrs, Laura Shemilt, Durgamadhab Mishra, Dirk Berger, Sören Selve, Dmitriy Mitin, Manfred Albrecht, and Stefan Eisebitt. A general approach to obtain soft x-ray transparency for thin films grown on bulk substrates. *Review of Scientific Instruments*, 88(10):103701, 2017.

[75] E. J. Candes, J. Romberg, and T. Tao. Robust uncertainty principles: exact signal reconstruction from highly incomplete frequency information. *IEEE Transactions on Information Theory*, 52(2):489–509, 2006.

[76] R. Chartrand. Exact reconstruction of sparse signals via nonconvex minimization. *IEEE Signal Processing Letters*, 14(10):707–710, 2007.

[77] Kuan He, Manoj Kumar Sharma, and Oliver Cossairt. High dynamic range coherent imaging using compressed sensing. *Opt. Express*, 23(24):30904–30916, November 2015.

[78] R. N. Wilke, M. Vassholz, and T. Salditt. Semi-transparent central stop in high-resolution x-ray ptychography using kirkpatrick-baez focusing. *Acta Crystallographica Section A: Foundations of Crystallography*, 69(Pt 5):490–497, September 2013.

[79] Richard L. Sandberg, Changyong Song, Przemyslaw W. Wachulak, Daisy A. Raymondson, Ariel Paul, Bagrat Amirbekian, Edwin Lee, Anne E. Sakdinawat, Chan La-O-Vorakiat, Mario C. Marconi, Carmen S. Menoni, Margaret M. Murnane, Jorge J. Rocca, Henry C. Kapteyn, and Jianwei Miao. High numerical aperture tabletop soft x-ray diffraction microscopy with 70-nm resolution. *Proceedings of the National Academy of Sciences*, 105(1):24–27, 2008.

[80] Stefan Schaffert, Bastian Pfau, Jan Geilhufe, Christian M Günther, Michael Schneider, Clemens von Korff Schmising, and Stefan Eisebitt. High-resolution magnetic-domain imaging by fourier transform holography at 21 nm wavelength. *New Journal of Physics*, 15(9):093042, sep 2013.

[81] Shashidhara Marathe, S. S. Kim, S. N. Kim, Chan Kim, H. C. Kang, P. V. Nickles, and D. Y. Noh. Coherent diffraction surface imaging in reflection geometry. *Optics Express*, 2010.

[82] Dennis F. Gardner, Bosheng Zhang, Matthew D. Seaberg, Leigh S. Martin, Daniel E. Adams, Farhad Salmassi, Eric Gullikson, Henry Kapteyn, and Margaret Murnane. High numerical aperture reflection mode coherent diffraction

microscopy using off-axis apertured illumination. *Opt. Express*, 20(17):19050–19059, Aug 2012.

[83] Michael Zürch, Christian Kern, and Christian Spielmann. Xuv coherent diffraction imaging in reflection geometry with low numerical aperture. *Optics Express*, 21:21131–21147, 2013.

[84] P. L. Combettes. The foundations of set theoretic estimation. *Proceedings of the IEEE*, 81(2):182–208, 1993.

[85] J. R. Fienup. Phase retrieval algorithms: a comparison. *Appl. Opt.*, 21(15):2758–2769, August 1982.

[86] D Russell Luke. Relaxed averaged alternating reflections for diffraction imaging. *Inverse Problems*, 21(1):37–50, November 2004.

[87] Veit Elser. Phase retrieval by iterated projections. *J. Opt. Soc. Am. A*, 20(1):40–55, January 2003.

[88] Yu.M. Bruck and L.G. Sodin. On the ambiguity of the image reconstruction problem. *Optics Communications*, 30(3):304 – 308, 1979.

[89] Bates R. Fourier phase problems are uniquely solvable in more than one dimension. i: Underlying theory. *Optik*, 1982.

[90] M. Hayes. The reconstruction of a multidimensional sequence from the phase or magnitude of its fourier transform. *IEEE Transactions on Acoustics, Speech, and Signal Processing*, 30(2):140–154, 1982.

[91] J. Miao, D. Sayre, and H. N. Chapman. Phase retrieval from the magnitude of the fourier transforms of nonperiodic objects. *J. Opt. Soc. Am. A*, 15(6):1662–1669, Jun 1998.

[92] Veit Elser and R. P. Millane. Reconstruction of an object from its symmetry-averaged diffraction pattern. *Acta Crystallographica Section A*, 64(2):273–279, March 2008.

[93] R. Hosemann and S. N. Bagchi. On homometric structures. *Acta Crystallographica*, 7(3):237–241, March 1954.

[94] J. Miao and D. Sayre. On possible extensions of x-ray crystallography through diffraction-pattern oversampling. *Acta Crystallographica Section A*, 56(6):596–605, 2000.

[95] J. R. Fienup and C. C. Wackerman. Phase-retrieval stagnation problems and solutions. *J. Opt. Soc. Am. A*, 3(11):1897–1907, November 1986.

[96] S. Marchesini, H. He, H. N. Chapman, S. P. Hau-Riege, A. Noy, M. R. Howells, U. Weierstall, and J. C. H. Spence. X-ray image reconstruction from a diffraction pattern alone. *Phys. Rev. B*, 68:140101, October 2003.

[97] Chien-Chun Chen, Jianwei Miao, C. W. Wang, and T. K. Lee. Application of optimization technique to noncrystalline x-ray diffraction microscopy: Guided hybrid input-output method. *Phys. Rev. B*, 76:064113, August 2007.

[98] J. C. H. Spence, U. Weierstall, and M. Howells. Phase recovery and lensless imaging by iterative methods in optical, x-ray and electron diffraction. *Philosophical Transactions of the Royal Society of London. Series A: Mathematical, Physical and Engineering Sciences*, 360(1794):875–895, 2002.

[99] Felix Büttner, Ivan Lemesh, Michael Schneider, Bastian Pfau, Christian M. Günther, Piet Hessing, Jan Geilhufe, Lucas Caretta, Dieter Engel, Benjamin Krüger, Jens Viefhaus, Stefan Eisebitt, and Geoffrey S. D. Beach. Field-free deterministic ultrafast creation of magnetic skyrmions by spin-orbit torques. *Nature Nanotechnology*, 12(11):1040–1044, 2017.

[100] Ichiro Inoue, Taito Osaka, Kenji Tamasaku, Haruhiko Ohashi, Hiroshi Yamazaki, Shunji Goto, and Makina Yabashi. An x-ray harmonic separator for next-generation synchrotron x-ray sources and x-ray free-electron lasers. *Journal of synchrotron radiation*, 25(Pt 2):346–353, March 2018.

[101] Toru Hara, Yuichi Inubushi, Tetsuo Katayama, Takahiro Sato, Hitoshi Tanaka, Takashi Tanaka, Tadashi Togashi, Kazuaki Togawa, Kensuke Tono, Makina Yabashi, and Tetsuya Ishikawa. Two-colour hard x-ray free-electron laser with wide tunability. *Nature Communications*, 4(1):2919, December 2013.

[102] Benoît Mahieu, Enrico Allaria, Davide Castronovo, Miltcho B. Danailov, Alexander Demidovich, Giovanni De Ninno, Simone Di Mitri, William M. Fawley, Eugenio Ferrari, Lars Fröhlich, David Gauthier, Luca Giannessi, Nicola Mahne, Giuseppe Penco, Lorenzo Raimondi, Simone Spampinati, Carlo Spezzani, Cristian Svetina, Mauro Trovò, and Marco Zangrando. Two-colour generation in a chirped seeded free-electron laser: a close look. *Opt. Express*, 21(19):22728–22741, Sep 2013.

[103] David Gauthier, Primož Rebernik Ribič, Giovanni De Ninno, Enrico Allaria, Paolo Cinquegrana, Miltcho Bojanov Danailov, Alexander Demidovich, Eugenio Ferrari, Luca Giannessi, Benoît Mahieu, and Giuseppe Penco. Spectrotemporal shaping of seeded free-electron laser pulses. *Phys. Rev. Lett.*, 115:114801, Sep 2015.

[104] A.M. Maiden, M.J. Humphry, M.C. Sarahan, B. Kraus, and J.M. Rodenburg. An annealing algorithm to correct positioning errors in ptychography. *Ultramicroscopy*, 120:64 – 72, 2012.

[105] Pierre Thibault and Andreas Menzel. Reconstructing state mixtures from diffraction measurements. *Nature*, 494(7435):68–71, February 2013.

[106] Darren J. Batey, Daniel Claus, and John M. Rodenburg. Information multiplexing in ptychography. *Ultramicroscopy*, 138:13 – 21, 2014.

[107] Ruben A. Dilanian, Bo Chen, Garth J. Williams, Harry M. Quiney, Keith A. Nugent, Sven Teichmann, Peter Hannaford, Lap V. Dao, and Andrew G. Peele. Diffractive imaging using a polychromatic high-harmonic generation soft-x-ray source. *Journal of Applied Physics*, 106(2):023110, 2009.

[108] Bo Chen, Ruben A. Dilanian, Sven Teichmann, Brian Abbey, Andrew G. Peele, Garth J. Williams, Peter Hannaford, Lap Van Dao, Harry M. Quiney, and Keith A. Nugent. Multiple wavelength diffractive imaging. *Phys. Rev. A*, 79:023809, February 2009.

[109] Garth J. Williams, Harry M. Quiney, Andrew G. Peele, and Keith A. Nugent. Coherent diffractive imaging and partial coherence. *Phys. Rev. B*, 75:104102, March 2007.

[110] Stefan Witte, Vasco T. Tenner, Daniel W. E. Noom, and Kjeld S. E. Eikema. Lensless diffractive imaging with ultra-broadband table-top sources: from infrared to extreme-ultraviolet wavelengths. *Light: Science &Amp; Applications*, 3:e163, March 2014.

[111] Brian Abbey, Lachlan W. Whitehead, Harry M. Quiney, David J. Vine, Guido A. Cadenazzi, Clare A. Henderson, Keith A. Nugent, Eugeniu Balaur, Corey T. Putkunz, Andrew G. Peele, G. J. Williams, and I. McNulty. Lensless imaging using broadband x-ray sources. *Nature Photonics*, 5:420, June 2011.

[112] Bo Chen, Brian Abbey, Ruben Dilanian, Eugeniu Balaur, Grant van Riessen, Mark Junker, Chanh Q. Tran, Michael W. M. Jones, Andrew G. Peele, Ian McNulty, David J. Vine, Corey T. Putkunz, Harry M. Quiney, and Keith A. Nugent. Diffraction imaging: The limits of partial coherence. *Phys. Rev. B*, 86:235401, December 2012.

[113] D. H. Parks, X. Shi, and S. D. Kevan. Partially coherent x-ray diffractive imaging of complex objects. *Phys. Rev. A*, 89:063824, June 2014.

[114] L. W. Whitehead, G. J. Williams, H. M. Quiney, D. J. Vine, R. A. Dilanian, S. Flewett, K. A. Nugent, A. G. Peele, E. Balaur, and I. McNulty. Diffractive imaging using partially coherent x rays. *Phys. Rev. Lett.*, 103:243902, December 2009.

[115] L. Mandel and E. Wolf. *Optical Coherence and Quantum Optics.* Cambridge University Press, Cambridge, 1995.

[116] Max Born and Emil Wolf. *Principles of Optics: Electromagnetic Theory of Propagation, Interference and Diffraction of Light (7th Edition).* Cambridge University Press, 7th edition, 1999.

[117] J. N. Clark, X. Huang, R. Harder, and I. K. Robinson. High-resolution three-dimensional partially coherent diffraction imaging. *Nature Communications*, 3(1):993, August 2012.

[118] Randy A. Bartels, Ariel Paul, Hans Green, Henry C. Kapteyn, Margaret M. Murnane, Sterling Backus, Ivan P. Christov, Yanwei Liu, David Attwood, and Chris Jacobsen. Generation of spatially coherent light at extreme ultraviolet wavelengths. *Science*, 297(5580):376–378, 2002.

[119] R. A. Bartels, A. Paul, M. M. Murnane, H. C. Kapteyn, S. Backus, Y. Liu, and D. T. Attwood. Absolute determination of the wavelength and spectrum of an extreme-ultraviolet beam by a young's double-slit measurement. *Opt. Lett.*, 27(9):707–709, May 2002.

[120] G. Y. Rainich. Electrodynamics in the general relativity theory. *Transactions of the American Mathematical Society*, 27(1):106–136, 1925.

[121] S. Eisebitt, M. Lörgen, W. Eberhardt, J. Lüning, and J. Stöhr. Lensless x-ray imaging of magnetic materials: basic considerations. *Applied Physics A*, 80(5):921–927, February 2005.

[122] Ne-Te Duane Loh, Stefan Eisebitt, Samuel Flewett, and Veit Elser. Recovering magnetization distributions from their noisy diffraction data. *Phys. Rev. E*, 82:061128, December 2010.

[123] M. Faisal Beg, Michael I. Miller, Alain Trouvé, and Laurent Younes. Computing large deformation metric mappings via geodesic flows of diffeomorphisms. *International Journal of Computer Vision*, 61(2):139–157, February 2005.

[124] Ozan Öktem, Chong Chen, N. Onur Domaniç, P. Ravikumar, and C. Bajaj. Shape-based image reconstruction using linearized deformations. *Inverse Problems*, 33(3), 2017. QC 20170609.

[125] Barbara Gris, Chong Chen, and Ozan Öktem. Image reconstruction through metamorphosis. *Inverse Problems*, 36(2), 2020. QC 20200407.

[126] A. Sotiras, C. Davatzikos, and N. Paragios. Deformable medical image registration: A survey. *IEEE Transactions on Medical Imaging*, 32(7):1153–1190, 2013.

[127] Marián Fecko. *Differential Geometry and Lie Groups for Physicists*. Cambridge University Press, 2006.

[128] Martin Bauer, Sarang Joshi, and Klas Modin. Diffeomorphic density matching by optimal information transport. *SIAM Journal on Imaging Sciences*, 8(3):1718–1751, 2015.

[129] Ralf Hiptmair and Jingzhi Li. Shape derivatives for scattering problems. *Inverse Problems*, 34(10):105001, jul 2018.

[130] B.B. Avants, C.L. Epstein, M. Grossman, and J.C. Gee. Symmetric diffeomorphic image registration with cross-correlation: Evaluating automated labeling of elderly and neurodegenerative brain. *Medical Image Analysis*, 12(1):26 – 41, 2008. Special Issue on The Third International Workshop on Biomedical Image Registration – WBIR 2006.

[131] L. Risser, F. Vialard, R. Wolz, M. Murgasova, D. D. Holm, and D. Rueckert. Simultaneous multi-scale registration using large deformation diffeomorphic metric mapping. *IEEE Transactions on Medical Imaging*, 30(10):1746–1759, 2011.

[132] Stefan Sommer, François Lauze, Mads Nielsen, and Xavier Pennec. Sparse multi-scale diffeomorphic registration: The kernel bundle framework. *Journal of Mathematical Imaging and Vision*, 46(3):292–308, July 2013.

[133] Alain Trouvé and Laurent Younes. Metamorphoses through lie group action. *Foundations of Computational Mathematics*, 5(2):173–198, April 2005.

[134] Jennifer L. Mueller and Samuli Siltanen. *Linear and Nonlinear Inverse Problems with Practical Applications.* Society for Industrial and Applied Mathematics, Philadelphia, PA, 2012.

[135] Wojciech Śmigaj, Timo Betcke, Simon Arridge, Joel Phillips, and Martin Schweiger. Solving boundary integral problems with bem++. *ACM Trans. Math. Softw.*, 41(2), February 2015.

[136] M. W. Scroggs, T. Betcke, E. Burman, W. Śmigaj, and E. van 't Wout. Software frameworks for integral equations in electromagnetic scattering based on Calderón identities. *Computers & Mathematics with Applications*, 74(11):2897–2914, 2017. Proceedings of the International Conference on Computational Mathematics and Inverse Problems, On occasion of the 60th birthday of Prof. Peter Monk.

[137] T. Betcke, E. van 't Wout, and P. Gélat. Computationally efficient boundary element methods for high-frequency Helmholtz problems in unbounded domains. In D. Lahaye, J. Tang, and K. Vuik, editors, *Modern Solvers for Helmholtz Problems*, pages 215–243. Springer International Publishing, 2017.

[138] A Litman, D Lesselier, and F Santosa. Reconstruction of a two-dimensional binary obstacle by controlled evolution of a level-set. *Inverse Problems*, 14(3):685–706, jun 1998.

[139] M. El-Shenawee, O. Dorn, and M. Moscoso. An adjoint-field technique for shape reconstruction of 3-d penetrable object immersed in lossy medium. *IEEE Transactions on Antennas and Propagation*, 57(2):520–534, 2009.

Acknowledgements

I would like to express my gratitude to my supervisor, Anders Mikkelsen, for the guidance and advice over the past several years. You have made a large impact on my work and perspective as a scientist and person – thank you.

A big thanks to Stefan Eisebitt and Bastian Pfau for introducing me to synchrotron and free electron laser experiments and for the supervision throughout my PhD work. The beamtimes and discussions have been an inspiration for me and have given me much to work on during my time as a PhD student.

I would like to thank Anne L'Huillier and Per Johnson for welcoming me into your group and providing me with valuable suggestions during my time there. I am constantly impressed with the dedication and quality of the members in your groups and it is clear that a big part of this is due to such good leadership.

Pablo Villanueva-Perez, thank you for the advice over the past several years including on various articles and imaging ideas. I have really enjoyed our discussions which often left me with a new perspective on the problem.

I would like to thank Andrea Troian and Foqia Rehman for being great office mates and Ren Zhe, Danny Mannix, Payam Shayesteh, Olesia Snezhkova, Olof Persson, Martin Hjort, Edvin Lundgren, Stacey Sorensen at the Synchrotron division who have made my time there enjoyable. Thank you to Patrik Wirgin and Anne Petersson-Jungbeck for all the help with everything economic and administrative related and to Håkan Ivansson for turning my rough sketches into realities. Thank you to the people in the 10 Hz group: Piotr Rudowski, Hampus Wikmark, Sylvain Maclot and Jasper Peschel for the help during the imaging experiments and making the lab such a fun environment. Thanks to collaborators: Michael Schneider, Peit Hessing, Felix Willems and Christian Günther who have made beamtimes enjoyable and to Edwin Fohtung for the interesting discussions related to coherent imaging.

I would like to thank the contributors to the following free and open source software: Debian GNU/Linux, Latex, Texstudio, Jabref, Inkscape, Atom, Paraview, Thun-

derbird, Firefox, Jupyter, Ipython and various Python packages such as: Numpy, Scipy, Matplotlib, Fenics, Bempp, Sympy, H5py, and scikit-image. I would like to thank Swedish National Infrastructure for Computing (SNIC) at Lunarc for access to the computational resources and to Joachim Hein for the technical assistance and installation of various software packages.

A special thanks to my parents, family, and to Jovana Colvin for their support and patience over the years. Jovana, the chaos of our many trips together have given me the optimism and laughter to (finally) finish this thing – thank you.

Summary of Papers

Paper I: Singleshot polychromatic coherent diffractive imaging with a high-order harmonic source

An imaging system was described for singleshot coherent diffractive imaging using a high intensity HHG source. The theory behind the multi-wavelength diffraction data was developed and was used to extract coherence properties about the source from double-slit diffraction data. The forward model was validated by comparing the computed diffraction patterns with the measured data and the extracted spectrum was used to calculate quasi-monochromatic diffraction patterns which were then input into different reconstruction algorithms for recovering the exit surfaces waves from the sample.

I was involved in constructing the experimental setup, acquiring and analyzing the data, and was the main responsible for writing the paper.

Paper II: Multi-wavelength phase retrieval for coherent diffractive imaging

A phase retrieval algorithm is described which is capable of recovering the exit surface wave associated with each wavelength within a multi-wavelength diffraction pattern. Through the adaptation of the constraint ratio, limits are placed on the number of wavelengths and the sample support shape. This is followed by numerical simulations which illustrated these limitations and the algorithm performance under different circumstances.

I developed the concept and algorithm, performed the analysis, and was main responsible for writing the paper.

Paper III: Phase retrieval via non-rigid image registration

In this paper, non-rigid image registration was developed and investigated as a potential phase retrieval method. The theory and algorithm were derived using concepts from exterior calculus which allowed different actions to be treated within the same framework. The images were treated as either functions or densities which results in the geometric and mass-preserving algorithms. Several numerical simulations are presented which illustrate the performance compared to the direct LDDMM registration algorithm as well as an iterative phase retrieval algorithm based on the ER and HIO algorithms.

Paper IV: Reference shape effects on Fourier transform holography

This paper investigated the effect that a thick reference aperture has on the reconstruction within a X-ray Fourier holography experiment. Using phase retrieval, we were able to compare the near and far fields between experiment and numerical multislice simulations. The multislice simulations were used to gain insight into various aspects related to the reconstruction process, such as the photon throughput, the spatial resolution and reconstruction plane for different geometries. These insights help to better understand the reconstruction process and provide guidance for fabricating references in order to optimize the quality of the reconstruction.

I analyzed the data, and was main responsible for writing the paper.

Paper V: 2D and 3D nanoscale imaging using high repetition rate laboratory-based soft X-ray sources

This work presented experimental results on several 2D and 3D imaging experiments. The tomography experiment utilized a plasma-based source to obtain 3D reconstructions of a diatom. The coherent diffractive imaging experiment used a soft X-ray laser to image a puzzlepiece test sample. The final synchrotron experiment performed Fourier holography which used a diffractive optical element to produce the sample illumination and reference waves in order to reconstruct an extended test sample.

I was involved in data acquisition and analysis in the coherent diffractive imaging experiment, and took part in writing the paper.

Printed by Media-Tryck, Lund 2021 NORDIC SWAN ECOLABEL 3041 0903

LUND
UNIVERSITY

Lund University
Faculty of Science
Department of Physics
Division of Synchrotron Radiation Research

ISBN 978-91-7895-873-3